PROJECT CALADRIUS

Heavy-Lift Mobility Platform

Spring 2024 AME-261 Design Project

USC Viterbi

CALADRIUS

Length

154.2 ft

Wingspan

212.9 ft

Cruise Altitude

43,000 ft

Takeoff Distance

8,800 ft

Landing Distance

8,200 ft

Max Range

3,460 nmi

Cruise Speed

472 kts

Propulsion

GE9x x3

MTOW

407 ton

Cost

$1.86B

463L Pallets

48 ct.

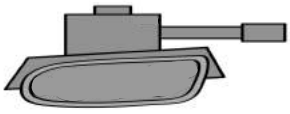

M1A2 Abrams

3 ct.

Passengers

440 ct.

Paratroopers

105 ct.

Pallets / M1A2 Abrams / Passengers / Paratroopers not included with initial purchase

Project Caladrius

Karan B., Jonah C., Nicholas L., Ilce M., Sofia P., and David S.

University of Southern California, Los Angeles, California, 90089, United States of America

Contents

Nomenclature

AR	=	Aspect Ratio
APU	=	Auxiliary Power Unit
BFL	=	Balanced Field Length
BPR	=	Bypass Ratio
B	=	Wheelbase
b	=	Span
BWB	=	Blended Wing Body
CFR	=	Code of Federal Regulations
CG	=	Center of Gravity
CFRP	=	Carbon Fiber Reinforced Polymer
CVR	=	Cockpit Voice Recorder
C_D	=	Coefficient of Drag
C_L	=	Coefficient of Lift
C_p	=	pressure coefficient
c	=	Chord
DATCOM	=	United States Air Force Stability And Control Digital DATCOM
d	=	Distance
D	=	Drag
δ_0	=	Pressure Ratio
e	=	Oswald Efficiency Factor
ECAS	=	Engine Crew Alert System
ENG	=	Engine
ETOPS	=	Engines Turn or Passengers Swim
FAR	=	Federal Aviation Regulations
FADEC	=	Full Authority Digital Engine Control
FDR	=	Flight Data Recorder
FMS	=	Flight Management System
FO	=	First Officer
g	=	Gravitational Acceleration on Earth
Λ	=	Wing Sweep Angle
γ	=	Descent/Climb Angle
GPS	=	Global Positioning System
GRD	=	Ground
h	=	height
HUD	=	Heads Up Display
HLA	=	Heavy Lift Aircraft
ICAO	=	International Civil Aviation Organization
ISA	=	International Standard Atmosphere
KIAS	=	Knots Indicated Airspeed
KTAS	=	Knots True Airspeed
L	=	Lift
LNAV	=	Lateral Navigation
M	=	Mach Number
m	=	Mass
MAC	=	Mean Aerodynamic Chord
M_a	=	Main Gear Distance to Aftmost CG
M_f	=	Main Gear Distance to Forwardmost CG
MBT	=	Main Battle Tank
MCP	=	Main Control Panel
MLOW	=	Maximum Landing Weight
MTOM	=	Maximum Takeoff Mass
MTOW	=	Maximum Takeoff Weight
N_a	=	Nose Gear Distance to Aftmost CG
N_f	=	Nose Gear Distance to Forwardmost CG
ND	=	Navigation Display
PACK	=	Pressurization Air Conditioning Kits
PFD	=	Primary Flight Display
ϕ	=	Ground Effect Induced Drag Correction
PTU	=	Power Transfer Unit
q	=	Dynamic Pressure
RAT	=	Ram Air Turbine
Re	=	Reynold's Number
ρ	=	Density
RTO	=	Rejected Takeoff
RoC	=	Rate of Climb
S	=	Wing Planform Area
SAM	=	Surface to Air Missile
SAF	=	Sustainable Aviation Fuel
σ	=	Density Ratio
T	=	Thrust
θ_0	=	Temperature Ratio
TSFC	=	Thrust-Specific Fuel Consumption
VNAV	=	Vertical Navigation
W	=	Weight
ZFW	=	Zero Fuel Weight

V-Speeds

V_1	=	Takeoff Decision Speed
V_a	=	Maneuvering Speed
V_{EF}	=	Takeoff Engine Failure Speed
V_{Lo}	=	Takeoff Liftoff Speed
M_{mo}	=	Maximum Mach Number
V_{mo}	=	Maximum Operating Speed
V_{ne}	=	Never Exceed Speed
V_r	=	Takeoff Rotation Speed
V_{ref}	=	Approach Speed
V_{stall}	=	Stall Speed
V_y	=	Best Rate of Climb Speed
V_x	=	Best Angle of Climb Spee

1 Introduction

The United States Air Force (USAF) Air Mobility Command operates at the forefront of global transportation, facilitating the rapid deployment and sustainment of forces worldwide. The command's central assets, the C-17 and the C-5M, demonstrate formidable capabilities. However, these aircraft are entering a maturity phase, necessitating foresight and innovation to maintain readiness and effectiveness. The re-engineered C-5M extends the lifespan of the fleet until the 2040s, yet the USAF must proactively plan for the eventual retirement of these aircraft to avoid capability gaps. Project Caladrius aims to address this challenge through the development of a next-generation heavy-lift aircraft utilizing the Blended Wing Body (BWB) concept. Scheduled to enter service in 2030, the aircraft will surpass the competition in transport capabilities, offering the capacity to carry three M1A2 Abrams tanks, 48 463L pallets, or 430 personnel, along with 105 paratrooper seats. This design merges traditional and innovative approaches to achieve a balanced solution. The BWB aircraft introduces several advantages aligned with the requirements of modern military transport. The integrated fuselage and wing structure enhance aerodynamic efficiency and fuel economy while providing ample internal space for the envisioned payload capacity of up to 430,000 lbs. Additionally, the distributed lift characteristics inherent to the BWB design offer stability and maneuverability critical for diverse operational environments. By embracing the BWB design, Project Caladrius aims to set a new standard in heavy-lift capability for the USAF's Air Mobility Command, ensuring superior readiness and effectiveness in global transportation operations.

Target market

The target market for heavy-lift aircraft includes government organizations such as the USAF and commercial entities requiring large-scale transportation for cargo and passengers. Many existing heavy-lift aircraft serve dual purposes, supporting both commercial and passenger transport, suggesting a potential direction for Caladrius to cater to a range of transportation needs. Figure 1 shows a trend in which larger aircraft carry substantial loads over extended distances, highlighting the demand for versatile aircraft capable of meeting diverse operational requirements. Caladrius's design, based on the Blended Wing Body (BWB) concept, offers greater lift and enhanced aerodynamic efficiency, boosting overall performance and fuel economy.

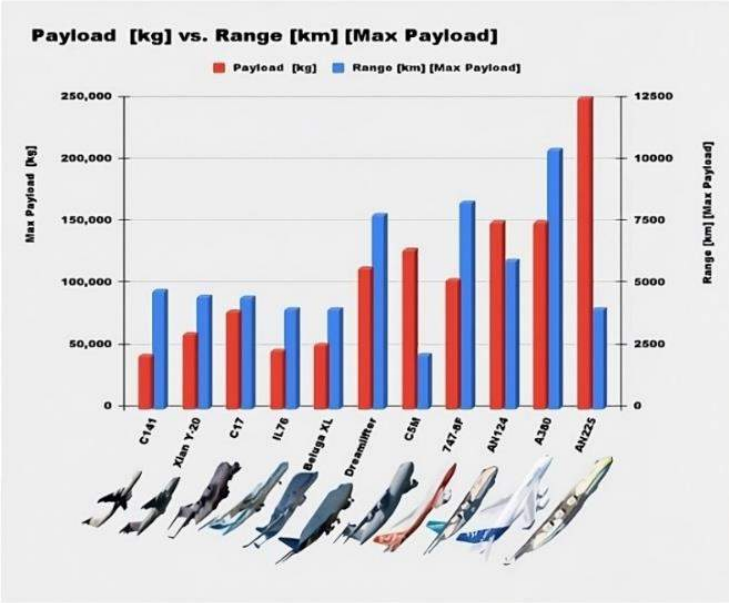

Figure 1: Payload and Ranges of Comparable HLA

This innovative approach allows Caladrius to excel in various transport functions, establishing a niche in the market and potentially setting a new standard in heavy-lift aircraft technology. By addressing the evolving demands of the target market, Caladrius could play a transformative role in shaping the future of global transport, offering cutting-edge solutions to complex logistics challenges and paving the way for more efficient and effective operations across both military and commercial sectors.

2 Design Missions

2.1 Design Requirements

The fundamental requirements for this heavy-lift aircraft (HLA) are to be able to carry a 430,000-lb payload with an unrefueled range of at least 2,500 nm (as well as a smaller 295,000-lb payload over a range of 5,000 nm). These payload requirements are to accommodate three M-1 Abrams Main Battle Tanks (MBT) while increasing range capabilities compared with the C-5M aircraft. Additional payload volume requirements dictate provisions to carry forty-eight 463L pallets and 430 passengers or paratroops across two passenger decks or compartments. Because the design requirements emphasized improved payload requirements compared to existing aircraft, the optimization metric used to design their aircraft was the unrefueled range at maximum payload.

Additional mission-specific performance requirements listed in Table 1 were outlined.

Table 1: Summary of Performance Requirements for the Aircraft Design

Requirement	430,000-lb Mission	295,000-lb Mission	Ferry Mission
Range (+ reserves)	2,500 nm	5,000 nm	8,000 nm
Velocity	≥ Mach 0.8 and ≤ Mach 0.82	≤ Mach 0.82	
Altitude	Initial cruise altitude from MTOW takeoff of at least 31,000 ft Service Ceiling of at least 43,000 ft at any weight configuration		
Takeoff	Operate on a 9,000 ft runway at sea level, ISA+15℃ conditions		

2.2 Theoretical Presentation

The drag coefficient of an aircraft is the sum of the parasitic and induced components of drag given by

$$C_D = C_{D,0} + C_{D,i} + \Delta C_D$$

where ΔC_D is the compressible drag correction found as a function of the lift coefficient, wing thickness to chord, and wing sweep that is nonzero as the freestream Mach number approaches the transonic regime. Because the mission requirements dictate a cruise speed of at least Mach 0.8, the compressible drag correction was considered in this analysis. The lift coefficient in steady level flight is computed by

$$C_L = \frac{2W}{\rho V^2 S}$$

The maximum ratio of the lift and drag coefficients for an aircraft, E_m, is an important aircraft design parameter as it can characterize aircraft performance in numerous flight regimes. The maximum lift to drag ratio can be computed explicitly for an aircraft design by

$$E_m = \sqrt{\frac{\pi e AR}{4C_{D,0}}}$$

The minimum drag and the minimum drag speed for the aircraft can then be found by

$$D_{min} = \frac{W}{E_m}$$

$$V_{D_{min}} = \sqrt{\frac{2W}{\rho S\left(\pi e AR C_{D,0}\right)^{1/2}}}$$

which specifies the conditions at which the endurance of a jet aircraft will be maximum. The maximum range of a jet aircraft is function of the ratio of $\sqrt{C_L}/C_D$, which is maximized when $3C_{D,0} = C_{D,i}$. In these conditions, the coefficient of lift is given by,

$$C_L = \sqrt{\frac{1}{3}\pi e A R C_{D,0}}$$

from which the maximum range at a constant airspeed and altitude and the corresponding ideal airspeed can be computed by

$$X = \frac{2VE_m}{(TSFC)_j}\tan^{-1}\left(\frac{W_0^*\zeta}{1+W_0^{*2}(1-\zeta)}\right) \quad (1)$$

$$W_0^* = \frac{W_0}{\sqrt{\pi e A R C_{D,0}}qS}$$

$$V_{X_{max}} = \sqrt{\frac{2W_0(1-\zeta)}{\rho S\sqrt{\frac{1}{3}\pi e A R C_{D,0}}}}$$

where $(TSFC)_j$ is the thrust specific fuel consumption for a jet engine, ζ is the fuel fraction for the cruise segment of flight, and W_0 is the initial aircraft weight at the start of cruise. These equations highlight the key parameters which this design must focus on: a maximization of $\left(\frac{\sqrt{C_L}}{C_D}\right)_{max}$ because of the importance of range in the mission requirements, a minimization of $C_{D,0}$, and a maximization of the fuel fraction ζ by minimizing the empty weight of the aircraft while providing adequate space to store the fuel.

2.3 Configuration Downselect

To begin the aircraft design, two down selects were conducted trading the high-level wing configuration and primary aircraft material. Two conventional layouts (and a nonconventional blended wing body were traded for the wing configuration. Table 2 and Table 3 introduce the respective deselects.

Table 2: Wing Configuration

Figure of Merit	Weight	Straight LE and TE	Blended Wing	Swept
				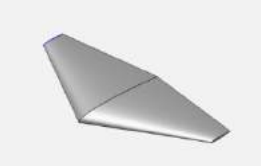
Stability	0.1	0	-1	1
Payload Capacity	0.3	0	1	-1
Community Noise	0.1	0	1	0
Aerodynamics	0.3	0	1	1
Manufacturability	0.2	0	-1	0
Total	**1**	**0**	**0.4**	**0.1**

The aircraft will have a blended wing design. One of the most significant benefits of choosing a blended wing was the increased aerodynamic efficiency. The traditional fuselage design generates large amounts of drag, while a blended wing with a decreased total wetted area [1] has a minimum skin drag. On top of that, a blended wing has high fuel efficiency and payload volume as this vehicle will need to travel effectively with heavy cargo and humans. Compared to traditional swept and rectangular wings, the most significant disadvantage to this design is decreased stability with no horizontal or vertical tail leading [2] so decreased longitudinal and directional stability. However, control surfaces will be incorporated to compensate for the instability of the blended wing design. As the blended wing body was selected, further down selects on traditional aircraft components such as a horizontal stabilizer were abandoned.

Table 3: Wing Material Selection

	Weight	Aluminum Alloys	Carbon Fiber	Steel
Figure of Merit		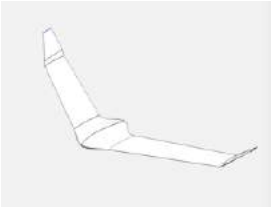		
Design Flexibility	0.1	0	1	-1
Fatigue Resistance	0.2	0	1	0
Strength	0.1	0	1	1
Brittleness	0.2	0	-1	1
Weight	0.3	0	1	-1
Cost	0.1	0	-1	0
Total	**1**	**0**	**0.4**	**-0.1**

Carbon fiber was chosen for the aircraft's body as it does not corrode compared to other alternatives like aluminum alloys or steel. On top of that, it has an optimal stiffness-to-weight performance, resulting in fewer parts needing to be manufactured [4]. It also would leave a smoother finish to reduce drag compared to the alternative. Although it is not as repairable, more brittle, and costs more [5], its effectiveness and lightweight properties were prioritized. Note that more discussion on carbon fiber selection and design is elaborated on in Section 8.

2.4 Design Mission and Trade Studies

Caladrius was initially sized using the method of constraint analysis and mission analysis. The results from these studies can also be parametrically varied to yield sensitivity results for thrust-to-weight ratio T/W and wing loading W/S. For detailed analysis and trade studies, a time-based simulator of a mission profile was written in Python. This allowed for higher-fidelity and higher-breadth investigations of the design space. These methods and their results are explored below.

To evaluate the design space of Caladrius, the performance constraints as published in the design requirements were evaluated using the method of constraint analysis. The primary goal of this method is to determine two key performance parameters of the aircraft: the thrust-to-weight ratio T/W and the wing-loading W/S. This can be done by deriving expressions that involve the performance metric in question as well as these two parameters. A diagram can then be created with lines of T/W and W/S that satisfy the performance constraint.

These expressions were taken from Gudmundsson [6]. Note that a few assumptions must be made. Namely, a rough guess of the minimum drag coefficient as well as drag and lift during take-off must be made. Also, for the

climb-related constraints, an estimate of the best rate of climb airspeed, V_y, must be made. A take-off drag coefficient and lift coefficient of 0.04 and 1.4, respectively, were used. These are suggested in Raymer [7] and Gudmundsson [6z] a minimum drag coefficient between 0.02 and 0.025 is suggested, and a conservative 0.03 is used for the analysis below.

2.4.1 Takeoff Constraint

Equation *(2)* constrains T/W and W/S for a given ground roll:

$$\frac{T}{W} = \frac{1.21}{(g\rho C_{L_{max}})S_g}\left(\frac{W}{S}\right) + \frac{0.605}{C_{L_{max}}}(C_{D\,TO} - \mu C_{L\,TO}) + \mu \qquad (2)$$

Since only the total takeoff distance is constrained, it was initially estimated that the ground must be shown to be under 6,500' at an altitude of 1,800' to meet design requirements. Later analysis modeled the entire balanced field length requirement for aircraft certification.

2.4.2 Cruise Speed Constraint

The minimum cruising speed as per the design requirements is Mach 0.8 at the cruising altitude of at least 31,000ft in the heaviest configuration. The constraining expression, equation *(3)*, is shown below:

$$\frac{T}{W} = q_{cruise}C_{D_{min}}\left(\frac{1}{W/S}\right) + k\left(\frac{1}{q_{cruise}}\right)\left(\frac{W}{S}\right) \qquad (3)$$

However, at the altitudes of high tropospheric and lower stratospheric flight, the impact of reduced density must be considered. The density ratio at 31,000ft is around 0.30, meaning that at first order an engine operating at that altitude will produce only 30% of the installed thrust at sea-level. This increases the required thrust by an order of magnitude. To account for this, equation *(3)* is modified as shown below:

$$\frac{T}{W} = \left[q_{cruise}C_{D_{min}}\left(\frac{1}{W/S}\right) + k\left(\frac{1}{q_{cruise}}\right)\left(\frac{W}{S}\right)\right]\frac{1}{\sigma} \qquad (4)$$

Which places a significant constraint on the required thrust to weight ratio to maintain steady-level flight at 31,000ft.

2.4.3 Service Ceiling Constraint

A minimum service ceiling of 43,000ft is specified in the design requirements. A few best ROC speeds, V_Y, were assumed and varied. The constraining expression, equation *(5)*, for the service ceiling is shown below:

$$\frac{T}{W} = \frac{1.667}{V_Y} + \frac{q_{V_Y}}{(W/S)}C_{D_{min}} + \frac{k}{q_{V_Y}}\left(\frac{W}{S}\right) \qquad (5)$$

This, along with the cruising Mach number, are the primary performance constraints on the aircraft.

2.4.4 Selection of T/W and W/S

The constraints analyzed above can be put together to identify feasible regions of the design space. The selected design point will thus serve as a baseline that satisfies all basic performance requirements, from which detailed trade studies can take place. The full constraint analysis diagram is shown below and includes all previously studied performance constraints, selecting the most conservative options (lowest $C_{L_{max}}$, highest RoC, etc.). It also includes data from several similar aircraft analyzed. The selected design point shows the similarity between Caladrius and similar aircraft, a good indication:

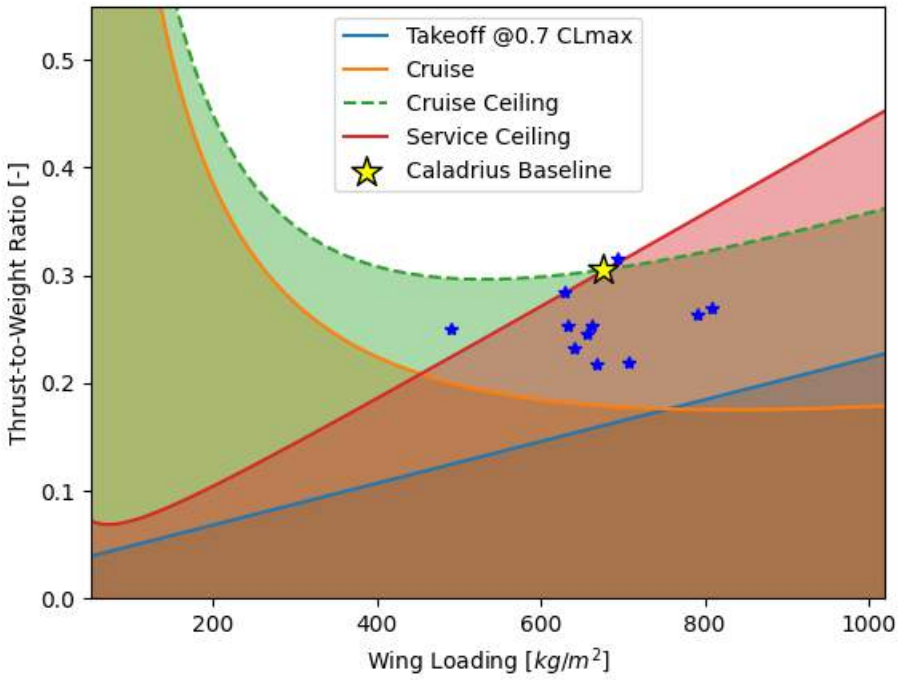

Figure Error! No text of specified style in document.**2:** Final Constraint Diagram

The initial design point for Caladrius is thus selected to be:

Table 4: Initial Design Point

Parameter	Initial Value
W/S	675 kg/m^2
T/W	0.3

And is labelled in the constraint diagram. These values can be parametrically varied to evaluate sensitivity to wing-loading and thrust-to-weight ratio. This is done by solving equations *(2)*Raymer [7] for the desired performance metric, and parametrically varying the thrust-to-weight ratio and wing loading in the expressions. The resulting carpet plots that show the sensitivity of the performance metrics are shown below:

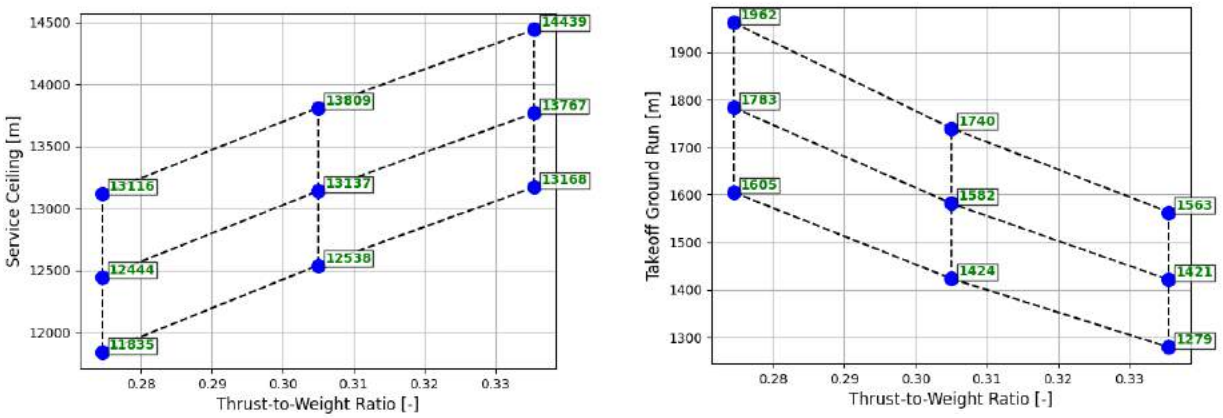

Figure 3: Caladrius Baseline-Parametric Sensitivity Studies

2.5 Preliminary Mission Analysis and Weight Sensitivity

2.5.1 Summary of Sizing Method

An initial value for the aircraft's takeoff gross weight W_0 was estimated using the method of mission analysis, explained at length in Gudmundsson [6] and Raymer [7]. An aircraft's take-off weight can be written as:

$$W_0 = \frac{W_c + W_p}{1 - \frac{W_e}{W_0} - \frac{W_f}{W_0}} \tag{7}$$

Known as the unity equation, where W_c and W_p are the crew and payload weights, specified in the RFP. The fraction $\frac{W_e}{W_0}$ is the empty weight fraction, which can be estimated by statistically fitting the empty weight versus the takeoff gross weight of aircraft of the same class in a power equation, such that:

$$\frac{W_e}{W_0} = AW_0^B$$

And the fuel fraction, $\frac{W_f}{W_0}$, can be estimated by analyzing the aircraft's design mission. A mission's *segment* is one "leg" of a mission, that is, the cruise, climb, descent, etc. Let W_i be the weight of the aircraft in segment i of a mission with N segments. Total fuel expenditure can be found by taking the product of all fuel fractions across the mission, that is:

$$\frac{W_f}{W_0} = 1 - \frac{W_1}{W_0}\frac{W_2}{W_1}\frac{W_3}{W_2}\frac{W_4}{W_3}\ldots = 1 - \prod_1^N \frac{W_i}{W_{i-1}}$$

Where the fuel fraction of each segment can be estimated using methods in the references cited above. Notice that solving for W_0 requires an iterative solution to the unity equation. The method can be further improved by guessing the increase in expected thrust-to-weight ratio in climb segments, $r_i = \frac{T_{max}}{W_0}\frac{W_0}{W_i}$ due to the fuel burn before that segment. Then, once a solution converges for W_0, these ratios can be re-computed with the actual weight at segment i, and the entire process repeated. This procedure is explained in detail in [9].

The methods in Raymer [7] and Gudmundsson [6] were incorporated into the sizing codes. The mission profile used is shown in the figure below:

Table 5: Caladrius Mission Profile Description

Mission Segment	Description	Performance Metrics
1 – 2	Taxi & Takeoff	-
2 – 3	Climb	SL to 31,000 ft MSL
3 – 4	Cruise	2500 nm M = 0.8
4 – 6	Descent/Loiter	45 minutes
7 – 8	Landing & Shutdown	-

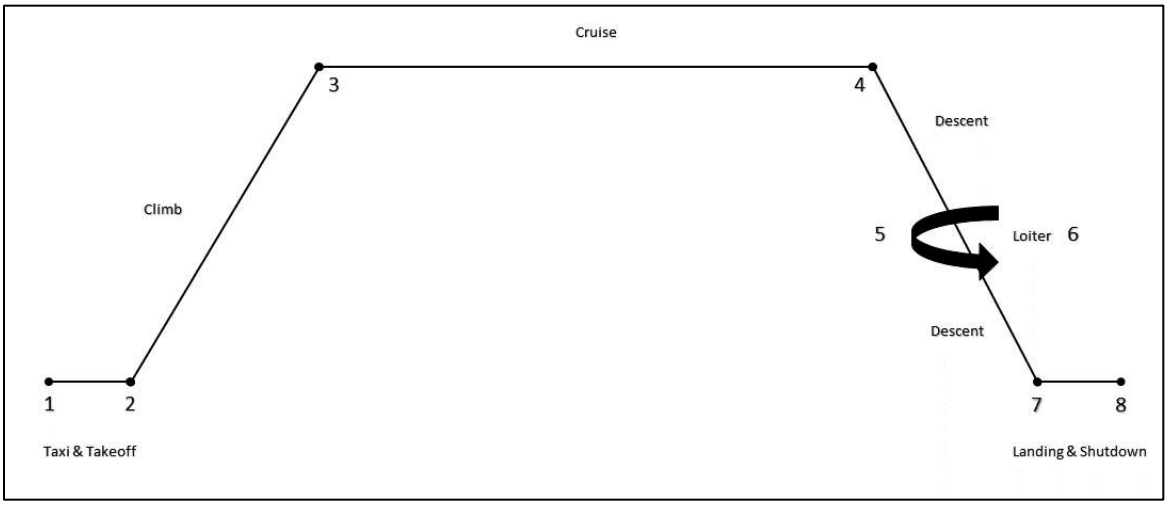

Figure 3: Caladrius Mission Profile

A few assumptions must be stated. First, a specific fuel consumption of $0.5/hr$ was assumed, reasonable for high-bypass ratio turbofans and in agreement with suggestions in Raymer [7] and Gudmundsson [6]. Additionally, Raymer [7] presents a method to estimate the maximum lift-to-drag ratio using a selected aspect ratio and a wetted area ratio, as shown in the equation *(8)*:

$$\left(\frac{L}{D}\right)_{max} = K_{LD}\sqrt{\frac{AR}{(S_{wet}/S_{ref})}} \tag{8}$$

The wetted area ratio can be "eyeballed" using a diagram provided in the textbook. One benefit of such configuration is clear here: its lower wetted area ratio (taken to be 2) allows for a more effective lifting body, yielding higher lift-to-drag ratio and improvements in performance. This comes with configuration and stability challenges.

The aspect ratio is selected, and an initial value of 10 is assumed based on similar aircraft [8]**Error! Reference source not found.**. A statistical fit method also in Raymer confirms the value. Finally, the empty weight fraction for the iterations is found with

$$\frac{W_e}{W_0} = 0.93W_0^{-0.07}$$

and the constants are found by statistical regression of similar aircraft, found also in Raymer [7].

2.5.2 Mission Analysis

The mission profile was analyzed iteratively. Below is the result of the iterations:

Table 6: Initial Weights

Parameter	Initial Value
W_0	407,442 kg
W_{empty}	145,141 kg
W_{fuel}	66,746 kg

3 Trade Studies

3.1 Mission Analysis

The aircraft mission consisting of 4 distinct segments used for parametric optimization is shown in Figure X. The ground segment consists of takeoff only; taxi fuel burn was neglected because the duration of the taxi—and therefore the total fuel burn on the ground—is small compared to the overall duration of any of the other flight segments. The climb was modeled as the most fuel efficient (economical climb) at minimum drag to an initial cruising altitude of at least 9,500 m (31,000 ft) per design requirements. The cruise segment was modeled as a constant altitude and velocity cruise at Mach 0.8 for the maximum payload mission and as a step climb cruise for the other missions (where the aircraft will climb at 2,000 ft increments as its weight decreases). The loiter segment was simulated as a 45 minute loiter at 3,000 m (10,000 ft) at the International Civil Aviation Organization (ICAO) maximum holding indicated airspeed of 230 KIAS (below 14,000 ft MSL) for a conservative [8] fuel burn estimate. Descent was not traded because the overall fuel burn and range contributions of the descent segment would be small compared to the climb, cruise, and loiter portions. Similarly, landing was not traded (though landing performance for the designed aircraft will be presented) because the minimum runway operating dimensions are more restrictive for takeoff than landing and therefore are not necessary to trade.

All segments were modeled through time-based numerical integration of the appropriate equations of motion to capture dynamic performance behavior and were validated against analytical models (Appendix B). All models use the Runge-Kutta method of order 5(4) [9] in Python [10]. The following subsections describe the assumptions, equations of motion, and limitations of each model in more detail.

3.1.1 Takeoff

During takeoff, the aircraft is modeled as undergoing one-dimensional linear acceleration in a horizontal plane starting initially at rest ($x = 0$, $\frac{dx}{dt} = 0$, $\frac{d^2x}{dt^2} = 0$). The takeoff is modeled at sea level using ISA+15℃ conditions (density altitude of approximately 550 m MSL, or 1,800 ft MSL) using the requirements of 14 CFR § 25.111 [11]. Namely, an engine is assumed to fail instantaneously at an engine failure speed, V_{EF}, equal to V_1. V_1 is determined iteratively for each design by starting with an assumed V_1 of 70% of the rotation speed V_r. Then, for each V_1, the stopping distance using maximum braking and no reverse thrust, d_{stop}, and the total distance to clear a 35 ft obstacle with one engine inoperative, d_{tko}, are computed. A one-second pilot reaction time is assumed between the failure of the engine and the application of braking for the rejected takeoff (RTO) [7]. For an appropriately selected V_1, d_{stop} and d_{tko} should be equal.

For the takeoff run, the equations of motion are:

$$\frac{dx}{dt} = v$$

$$\frac{dv}{dt} = \frac{1}{m}[T - D - (mg - L)]$$

where D is the total aerodynamic drag with $C_L = 0.7C_{L_{max}}$ (refer to Section 3.3 for drag models), T is the total thrust (with either all engines operative or for velocities greater than V1, one engine inoperative) computed using the Mattingly thrust model (refer to Section 3.4 for thrust models), and L is the lift with $C_L = 0.7C_{L_{max}}$ given by $L = \frac{1}{2}\rho v^2 S C_{L_{max}}$. For the RTO portion, it is assumed that no reverse thrust is used, so $T = 0$, and $C_L = 0.3C_{L_{max}}$ (to simulate the deployment of spoilers).

The aircraft is assumed to become airborne at $V_{Lo} = 1.2V_{stall}$, and the airborne climb segment was assumed to be flown at V_{Lo}. With these assumptions, the total horizontal distance covered to clear an obstacle of height $h_{obst}$is approximated by

$$x = h_{obst}\left(\frac{W}{T - D}\right)$$

where T and D are evaluated at V_{Lo}. The distance covered during the rotation was not modeled in this program because V_r is typically $1.1V_{stall}$ with a climb speed of $1.2V_{stall}$, so the rotation distance is implicit in the ground roll computation [7].

After each iteration, a new value of V_1 is computed by $V_{1,new} = V_{1,old}\left(1 + \frac{d_{tko} - d_{stop}}{10000}\right)$, though V_1 cannot exceed V_r in accordance with 14 CFR § 25.107(e)(1)(i). A simulation converges when the difference between d_{tko} and d_{stop} is less than 1 meter (typically requiring about 10 iterations).

The takeoff distance is determined by 14 CFR § 25.113(a) as the greater of d_{tko} or 115% of the total takeoff distance (clearing a 35ft obstacle) with all engines operative, the latter of which is simulated as a single trial without any engine failures.

This numerical model was compared with an empirical model given in Raymer which gives the BFL as

$$BFL = \frac{0.8631}{1 + 2.3G}\left(\frac{\left(\frac{W}{S}\right)}{\rho g C_L} + h_{obst}\right)\left(\frac{1}{\frac{T_{av}}{W} - U} + 2.7\right) + \frac{655}{\sqrt{\frac{\rho}{\rho_0}}} \tag{9}$$

where

$$G = \sin^{-1}\left(\frac{T - D}{W}\right) - \gamma_{min}$$

$$U = 0.01 C_{L_{max}} + 0.02$$

$$T_{av} = 0.75T\left(\frac{BPR + 5}{BPR + 4}\right)$$

and γ_{min} is the minimum climb gradient specified in 14 CFR § 25.111(c)(3) as 0.024 for a 2-engine aircraft, 0.027 for a 3-engine aircraft, and 0.030 for a 4-engine aircraft. The time-based model tended to give a greater balanced field length at high takeoff weights (see Appendix B), so the time-based model was used in these trade studies for a conservative analysis.

3.1.2 Economical Climb

The climb segment was modeled with the aircraft at its minimum drag speed, which for a jet aircraft is given by

$$V_{Dmin} = \sqrt{\frac{2W}{\rho S\sqrt{\pi e A R C_{D,0}}}} \tag{10}$$

until is achieves a freestream Mach of 0.8 (the cruise Mach), at which point the aircraft climbs at

$$V = 0.8a(T)$$

where $a(T)$ is the speed of sound at a given temperature in the International Standard Atmosphere. This conversion to a Mach-based climb is necessary due to the onset of compressible drag at higher Mach numbers and to remain below the maximum Mach number of the aircraft. 14 CFR § 91.117(a) requirements to maintain a maximum of 250 KIAS below 10,000 ft MSL were not instituted in this analysis because as a USAF aircraft, this HLA is not subject to 14 CFR Part 91 operating requirements, and such HLA aircraft are often required to exceed 250 KIAS below 10,000 ft to fly in a clean configuration.

The equations of motion for this segment are given by

$$\frac{dx}{dt} = V\left(1 - \left(\frac{T - D}{W}\right)^2\right)$$

$$\frac{dy}{dt} = V\left(\frac{T - D}{W}\right)$$

$$\frac{dW}{dt} = -T(TSFC)_j$$

where $\frac{dW}{dt} = \frac{dm_{fuel}}{dt}$ is the fuel burn rate and T is computed assuming the throttle is set to a climb throttle of 90%.

3.1.3 Constant Airspeed and Altitude Cruise

The cruise segment for the short, 2,500 nm mission was modeled as a FAR-compliant cruise at a constant altitude (at least 31,000 ft) and airspeed (Mach 0.8). The duration of the cruise was set by the required remaining fuel for the loiter (refer to Section 3.1.5).

The equations of motion for this segment are given by{

$$\frac{dx}{dt} = v$$

$$\frac{dW}{dt} = -D(TSFC)_j$$

The analytical model for a jet cruising at a constant altitude and airspeed is given by Eq. 1. The time-based model was used for trade studies because it more accurately captured dynamic behaviors involving drag, where the compressible and induced portions are functions of the coefficient of lift, which varies with the weight of the aircraft in steady, level flight. See Appendix B for a more detailed discussion.

3.1.4 Step Climb Cruise

For the longer missions (5,000 nm payload mission and ferry mission), a step climb model was used to maximize range. As the weight of the aircraft decreases, it is advantageous to cruise at a higher altitude (lower density) due to decreased fuel burn. A sample flight profile with a step climb cruise is shown in Figure 4

Each intermediate cruise segment was modeled as a constant altitude and velocity cruise (Section 3.1.3) while each intermediate climb was modeled as a constant Mach climb. The aircraft climbs to a higher altitude in 2,000 ft increments once it computes that it is more economical to cruise at the higher altitude (lower thrust required). The cruise terminates once the fuel remaining equals the loiter fuel requirement.

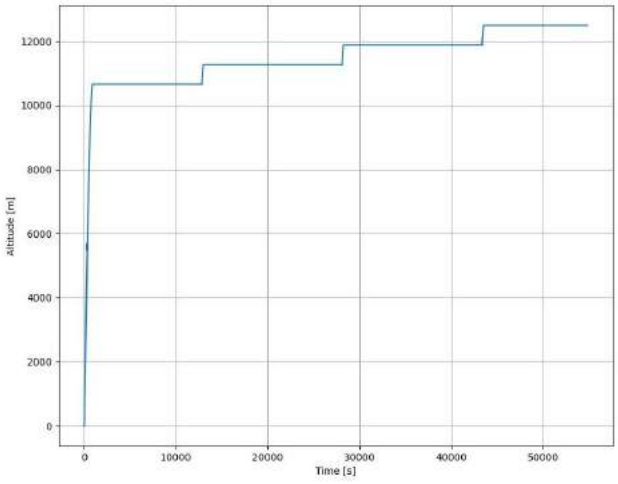

Figure 4: Sample Step Climb Mission

3.1.5 Loiter

The loiter segment is a constant altitude and velocity cruise at the lower altitude of 10,000 ft MSL to simulate holding prior to landing with the increased fuel burn of lower altitudes. The maximum ICAO authorized holding speed of 230 KIAS is assumed for a forty-five-minute holding period. This corresponds to a true airspeed of 137 m/s given by

$$KTAS = KIAS\sqrt{\frac{\rho_0}{\rho}} \qquad (11)$$

Because the loiter segment does not contribute to the overall range of the aircraft, only the fuel burn is integrated with negative time increments from zero fuel to find the fuel required to sustain a 45 minute loiter. The equation of motion is

$$\frac{dW}{dt} = -D(SFC)_j$$

3.1.6 Landing

While landing was not part of the trade study flight profile, the module is described here as it was used for landing performance analysis of the selected aircraft. Landing is modeled in three stages: a constant airspeed descent at an approach angle of 3 degrees, a flare maneuver modeled as a circular arc, and a time-based deceleration period on the ground. The horizontal distance flown during the descent phase is given in Raymer [7] as

$$x_{descent} = \frac{h_{obst} - h_{flare}}{\tan\gamma} \tag{12}$$

where h_{obst} is the height of the obstacle (50 ft in accordance with 14 CFR § 25.125(a)), h_{flare} is the height at which the flare maneuver is initiated given by

$$h_{flare} = R(1 - \cos\gamma)$$

γ is the descent angle, assumed to be 3 degrees, and R is the radius of the flare arc given by

$$R = \frac{V_{ref}^2}{0.2g}$$

The horizontal distance covered during the flare is given in Raymer [7] as

$$x_{flare} = R\sin\gamma \tag{13}$$

V_{ref} is assumed to be $1.3V_{stall}$ in accordance with 14 CFR § 25.125(b)(2). The aircraft velocity is then assumed to decrease during the flare maneuver to $1.15V_{stall}$ at touchdown.

The landing ground roll, x_{ground}, is computed by numerically integrating the following equations of motion:

$$\frac{dx}{dt} = v$$

$$\frac{dv}{dt} = -\frac{1}{m}\left(T_{rev} + D + (mg - L)\right)$$

where D and L are computed assuming a coefficient of lift of 0.3 (to simulate spoiler deployment) and the reverse thrust is assumed to be 25% of the maximum forward thrust under the given environmental conditions. Integration terminates when the velocity reaches zero, from which the landing distance can be determined as the sum of the distances given by Eq. 12, 13, and the distance x_{ground}.

To account for variable pilot technique, Raymer's [7] suggestion to multiply the total resulting horizontal distance by 1.667 as the landing distance figure is adhered to. This provides a conservative short field landing distance for the aircraft accounting to variation in pilot technique.

3.2 Weight Estimation

The weight buildup for a given BWB design was computed using the Bradley Prediction Model from Boeing's Flight Optimization Software. The maximum takeoff mass (MTOM) was assumed from the constraint analysis at 407,000 kg. The fuselage mass, m_{fus}, the mass of the center-body between the wings, m_{aft}, and the wing mass, m_{wing}, are given, in imperial units (lb_m), by

$$m_{fus} = \frac{5.698865n_{pax}}{450}(0.316422)(MTOM)^{0.166552}(S_{cabin})^{1.601158}$$

$$m_{aft} = 0.53\left(1 + 0.05N_{eng}\right)\left(S_{aft}\right)(MTOM)^{0.2}\left(\lambda_{aft} + 0.5\right)$$

$$m_{wing} = (0.8)(0.028)\left[\left(\frac{\sqrt{AR(S)^3}}{\cos\Lambda}\right)\left(\frac{1+2\lambda}{3+3\lambda}\right)\left(\frac{(MTOM)n_{struct}}{S}\right)^{0.3}\left(\frac{V_{dive}}{\left(\frac{t}{c}\right)_{ave}}\right)^{0.5}\right]^{0.9}$$

The number of passengers, n_{pax}, was assumed to be 430. Other non-structural weight estimates included the landing gear mass, given as a constant fraction of MTOM by

$$m_{lg} = 0.0445(MTOM)$$

the mass of the auxiliary-power unit (APU), also given as a fraction of MTOM by

$$m_{apu} = 0.001(MTOM)$$

the mass of instrumentation, including avionics and wiring, given by

$$m_{inst} = 0.4536\left(N_{eng}\left(5+\frac{0.01323(MTOM)}{1000}\right)+30+0.012214(MTOM)\right)$$

the mass of the hydraulic systems, given by

$$m_{hydro} = 3.2\sqrt{MTOM}$$

the mass of all air systems, including air conditioning/pressurization and anti/de-icing, given by

$$m_{ac} = 10.045\left(l_{fus}\right)^{1.28}$$

and the mass of the engines, given by

$$m_{eng} = 14.7\left(\frac{T}{1000}\right)^{1.1} e^{-0.045BPR}$$

For weight estimation, the thrust to weight ratio was selected from constraint analysis to be 0.3 with 4 engines. A bypass ratio (BPR) of 10 was assumed for a high-bypass turbofan engine. Note that the number of engines was later revised to 3 after propulsion-specific trade studies. The fuselage dimensions were based on the fuselage volume and floor area requirements to carry the mission payload and assumed to be a diameter of 10 m and a fuselage length of 46 m with a floor area, S_{cabin}, of 300 m^2. The sum of each of these masses gives the aircraft empty mass, or

$$m_{empty} = m_{fus} + m_{aft} + m_{wing} + m_{lg} + m_{apu} + m_{inst} + m_{hydr} + m_{ac} + m_{eng}$$

The payload weight consists of the crew (4 crew with 4 relief-crew for a total of 8 crew at 300 lb_f per crew member), which is assumed constant for all missions, and a variable cargo payload weight dependent on the mission specifications. Fuel weight was implicitly traded by assuming that the fuel weight was the difference between the maximum takeoff weight and the zero-fuel weight, ZFW, (sum of aircraft empty and payload weights). This assumption was justified by the abundance of fuel storage room in the wings. The maximum fuel weight was later determined based on the ferry mission requirements.

3.3 Drag Estimation

The coefficient of drag, C_D, in any flight regime is given in Eq. 14 as the sum of the parasitic, induced, and compressible components of drag,

$$C_D = C_{D,0} + C_{D,i} + \Delta C_D \qquad (14)$$

The parasite component of drag, $C_{D,0}$ was estimated for the aircraft as the sum of the contributions to friction drag of every wetted component. Assuming entirely turbulent flow with the Reynold's Number, Re, given by

$$Re_{fus} = \frac{v l_{fus}}{\nu} \qquad Re_{wing} = \frac{V\bar{c}}{\nu}$$

can then be used to the compute the skin friction coefficient, C_{fx}, for a component x by

$$C_{fx} = \frac{0.074}{(Re_x)^{0.2}}$$

The drag coefficient of fuselage alone is given by

$$c_{d,fus} = C_{f,fus}\left[1 + 1.5\left(\frac{l_{fus}}{d_{fus}}\right)^{-1.5} + 7\left(\frac{l_{fus}}{d_{fus}}\right)^{-3}\right]$$

The aircraft coefficient of parasitic drag is then computed by

$$C_{D,0} = \frac{c_{d,fus}S_{fus} + 2C_{f,wing}S}{S} \tag{15}$$

A ratio of total wetted area to wing area of 5 was used for all trade studies, and this value was assumed to include any additional perturbations (e.g. antennas). One major limitation of this parasite drag buildup is that it does not account for profile drag, so parasite drag estimates are likely underestimating the true drag buildup of the aircraft.

The induced component is computed as a function of the coefficient of lift by

$$C_{D,i} = \Phi k C_L^2 \tag{16}$$

where

$$\Phi = \frac{16\left(\frac{h}{b}\right)^2}{1+16\left(\frac{h}{b}\right)^2}$$

is the ground effect correction term considered nonsingular only during the takeoff and landing portions of the flight simulation, and $k = \frac{1}{\pi e AR}$. A constant Oswald efficiency of 1.0 was assumed for these trade studies due to the lack of an appropriate model of Oswald efficiency for BWB designs tradeable in these simulations. This higher Oswald efficiency was justified by BWB design being more aerodynamic compared to more conventional aircraft and through the incorporation of winglets in the design. Furthermore, the design space was considered small enough that any variation in actual Oswald efficiency between traded designs could be accounted for by winglet sizing to increase the effective aspect ratio with minimal drag or weight penalties.

The compressible correction factor, ΔC_D, was computed by

$$\Delta C_D = [(3.97 \times 10^{-9})e^{12.7x} + (10^{-40})e^{81x}]\cos^3\Lambda \tag{17}$$

where

$$\mathrm{x} = \frac{\mathrm{M}_\infty}{M_{cc,\Lambda=0}}\cos^m\Lambda$$

$$M_{cc,\Lambda=0} = 0.87 - 0.175C_L - 0.83\left(\frac{t}{c}\right)$$

$$m = 0.83 - 0.583C_L + 0.111C_L^2$$

Note that the compressible drag correction depends on two aircraft parameters: the wing sweep and airfoil thickness to chord ratio. These were not explicitly traded, but rather selected based on mission requirements and later validated through sensitivity analysis; the sweep was assumed as 35 degrees to maximize the range while adhering to manufacturability constraints, while the thickness to chord ratio was selected as 0.13 to maximize the wing volume for fuel while not significantly increasing the compressible drag effects at the target cruise of Mach 0.8.

3.4 Thrust Model

A dynamic thrust model capturing variations in thrust with altitude and Mach number was desired. Mattingly's thrust model for high bypass-ratio turbofans was used [12] It has as inputs both flight and atmospheric conditions and returns the thrust-available based on those conditions.

The total available thrust per engine is given by

$$T_A = T_{SL}\delta_0\left[1 - 0.49\sqrt{M_\infty} - \frac{3(\theta_0 - TR)}{1.5 + M_\infty}\right] \text{ if } \theta_0 > TR \tag{18}$$

$$T_A = T_{SL}\delta_0\left[1 - 0.49\sqrt{M_\infty}\right] \text{ if } \theta_0 \leq TR \tag{19}$$

where the temperature ratio θ_0 and pressure ratio δ_0 are related to the sea-level T_0 and P_0, respectively, by

$$\theta_0 = \frac{T}{T_0}\left(1 + \frac{\gamma - 1}{2}M^2\right)$$

$$\delta_0 = \frac{P}{P_0}\left(1 + \frac{\gamma - 1}{2}M^2\right)^{\frac{\gamma}{\gamma - 1}}$$

from isentropic flow relations. The reference also provides models for installed thrust-specific fuel consumption (TSFC) as functions of altitude and Mach number. These are useful to dynamically vary the fuel consumption in flight, taking altitude effects into account. For high bypass-ratio turbofans, the variation in TSFC is given by

$$TSFC = (0.45 + 0.54M_\infty)\sqrt{\theta} \tag{20}$$

variations for an arbitrary engine are shown in the figure below:

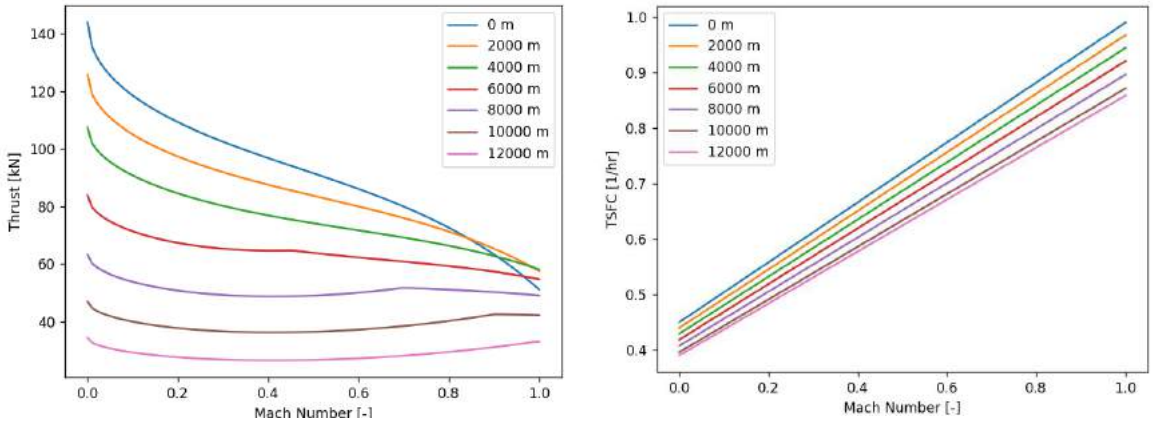

Figure 5: Range trade study varying aspect ratio and wing area.

3.5 Trade Studies

3.5.1 Wing Geometry

Trade studies were run to investigate the design space suggested by the preliminary constraint analysis. Initially, tradeable aerodynamic parameters affecting mission performance were identified as the wing area and the aspect ratio. Based on the constraint analysis, trade studies were running sweeping aspect ratios between 6 and 7 and wing areas between 580 and 700 m^2. Cruise velocity was not traded because it was constrained to being between Mach 0.8 and

0.82, and therefore this limited range would not provide exceptionally insightful results. The range results of a 3,600 aircraft sweep for the 2,500 nm payload mission are shown in Figure 6.

The results indicate a strong dependence on the wing area, with larger wing areas tending to have longer ranges. This is because larger wing areas allow the aircraft to cruise at a lower coefficient of lift, decreasing both the induced and compressible components of drag, which outweigh the increase in friction drag. However, for wing areas exceeding approximately 660 m^2, larger wing areas result in a decrease in range. This is because larger wing areas increase parasitic drag and increase the empty weight of the aircraft, decreasing the fuel load during this mission (because of the implicit trading of fuel with the constant MTOW). There is a dependence on aspect ratio, though not as strong as the dependence on wing area, with higher aspect ratios reducing induced drag and therefore increasing the range. However, higher AR designs have a weight penalty, making the dependence on AR weak. The stronger dependence on wing area than aspect ratio indicates that the decrease in compressible drag is likely the largest driving factor in range differences in this trade study.

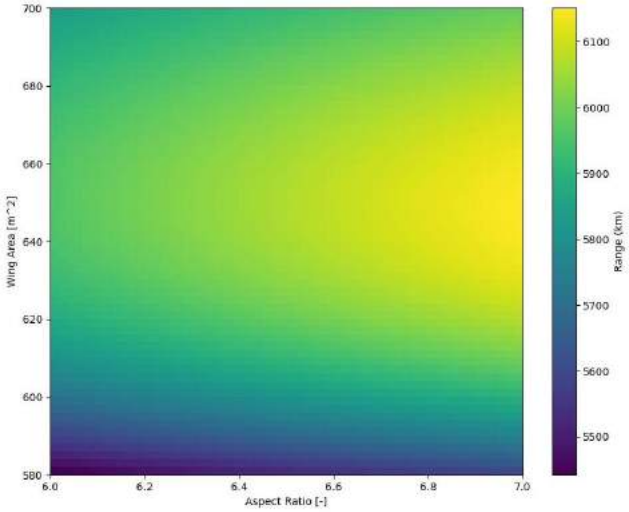

Figure 6: Range trade study varying aspect ratio and wing area.

Next, takeoff limitations were instituted. Figure 7 shows the BFL for aircraft in this study. The required field length depends inversely on both the aspect ratio and wing area. This fundamentally makes sense, as a larger wing area decreases the lift off velocity, while a larger aspect ratio decreases induced drag, increasing acceleration. Using the takeoff field length results, the design space was constrained by eliminating designs which exceed the maximum field length of 9,000 ft. The reduced design space is shown in Figure 8.

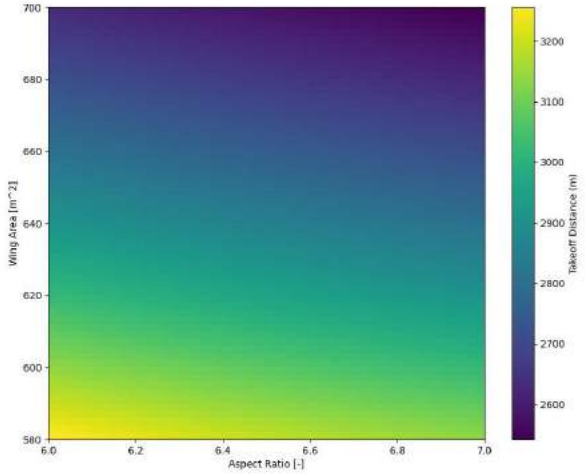

Figure 7: Takeoff Distances traded with Wing Area and Aspect Ratio

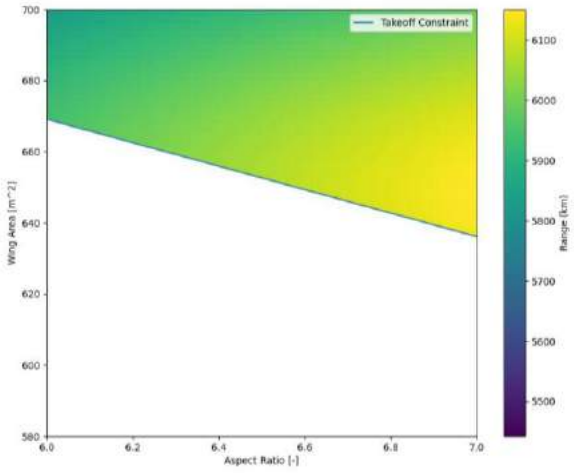

Figure 8: Range trade study with TOFL compliant designs.

The other missions did not constrain the design space any further; in other words, all these aircraft met all the remaining performance constraints regarding service ceiling (which depends primarily on the propulsion system and therefore is further analyzed during propulsion trades), 134,000 kg (295,000-lb) payload mission range, and the ferry mission range. This is because those missions do not have a minimum cruise speed requirement, and therefore a cruise at a more economical speed is possible.

One final logical constraint which can be implemented in these trade studies constrains the span of the aircraft. The current design space includes both ICAO Code E and F aircraft; however, it is advantageous to design an aircraft to a lower ICAO type designator because it increases the types and number of airfields at which their aircraft can operate. Constraining the design space to Code E aircraft (maximum wingspan of 65 m), the resulting design space is shown in Figure 9.

With the design space constrained, the aircraft was sized to lie near a local maximum in the design space, with an aspect ratio of 6.4 and a wing area of 659 m^2 (wingspan of 65 m). The loss in range by restricting the wingspan to ICAO Code E is approximately 100 km and therefore a justifiable tradeoff.

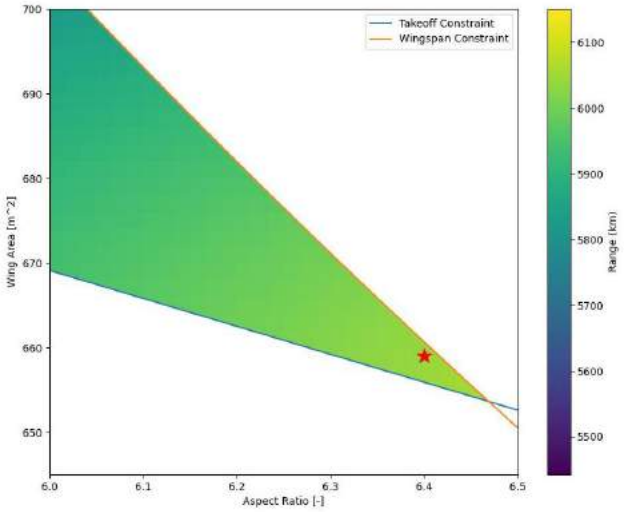

Figure 9: Trade study with the selected design.

Table X lists the weight estimation for this aircraft design, which justifies the estimated empty weight of this aircraft design. Note that the final weight buildup for the designed aircraft differs from these statistical estimates, and this table is presented only as a result of preliminary trade studies.

3.5.2 Weight Buildup

Table 7: Weight Buildup

Component	Mass (kg)
Fuselage (structural)	35,700
Wing (structural)	53,500
Landing Gear	18,100
APU	400
Instrumentation/Avionics	5,000
Hydraulics	2,000
Air Conditioning/Ducting	3,600
Engines	22,800

Empty Weight	141,000
Fuel (2500 nm Mission)	71,000
Fuel (Ferry Mission)	123,600

3.5.3 Sensitivity Study

The table below lists the assumed aircraft design parameters used for trade studies.

Table 8: Aircraft Design Parameters

Parameter	Assumed Value
Taper Ratio (λ)	0.3
Sweep (Λ)	35 deg.
$C_{L_{max}}$	2.0
(t/c)	0.13
BPR	10
$(T/MTOW)$	0.3

Using the aspect ratio and wing area selected from the wing geometry trades, the following sensitivity studies were conducted.

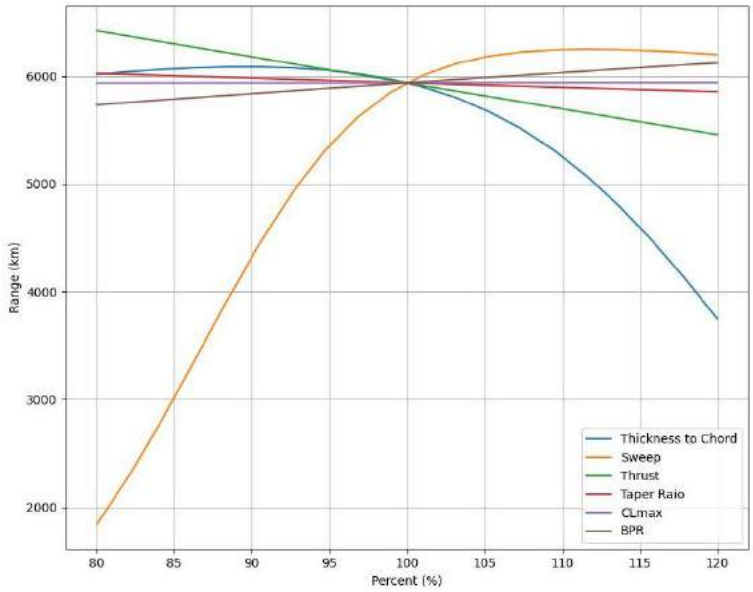

Figure 10: Range sensitivity study.

The range sensitivity study indicates a strong dependence on the wing sweep due to the high Mach cruise increasing compressible drag. Since airfoil type is not considered in their sensitivity analysis, using a supercritical airfoil can alleviate some of this sensitivity. However, wing sweeps above approximately 40 degrees have a weight penalty and therefore decreased range. The other most sensitive components are the airfoil thickness to chord ratio, also because of the compressible drag effects, and thrust, due to higher available thrust increasing the engine weight and decreasing fuel load. The wing taper ratio, $C_{L_{max}}$, and engine BPR have comparatively small effects on the range. Therefore, this study indicated that it was critical to achieve a wing sweep of 35 degrees and a thickness to chord ratio of approximately 0.13 to reduce compressible drag effects. While the sensitivity study indicated that a smaller thickness to chord ratio may increase range, the assumed value of 0.13 was kept to maximize wing volume for fuel requirements.

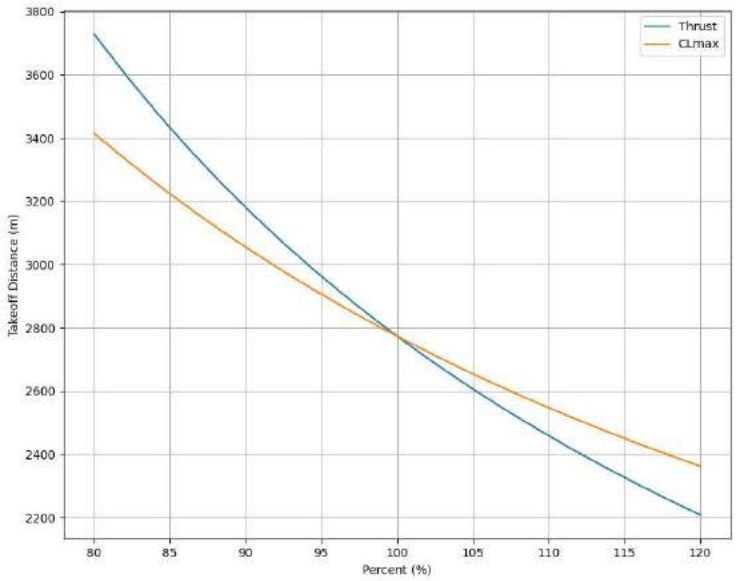

Figure 11: Takeoff distance sensitivity study.

The takeoff sensitivity study indicates strong dependence on both the available thrust and the $C_{L_{max}}$. Note that the other assumed parameters have minimal impact on the takeoff distance because, while they do impact the empty weight of the aircraft, the trade study assumes a variable fuel load with a constant takeoff weight at MTOW. Therefore, those parameters are omitted from Figure 10. The thrust requirement, since it is the most sensitive parameter for takeoff performance, was further investigated in a separate study (see Propulsion Study).

The requirement for a high $C_{L_{max}}$ of approximately 2.0 /was concerning because the swept wings required to achieve the range requirement are not conducive to high coefficients of lift due to spanwise flow. As such, high-lift devices are investigated in section 5 to achieve this higher lift coefficient requirement. Higher values of $C_{L_{max}}$ were ruled out as being infeasible even to justify in a conceptual analysis.

4 Propulsion Study

Several propulsion packages were investigated, consisting of both existing and future turbofan engines. Only high BPR turbofan engines were considered due to the high thrust and high fuel efficiency requirements, as dictated by the constraint analysis. Furthermore, only 3 and 4 engine configurations were considered due to the high thrust requirement and the advantage of not requiring ETOPs certification under 14 CFR Part 25.

Table 9: Traded Propulsion Packages

Engines	N_{eng}	Total Thrust (N)	TSFC $(N_{fuel}/N\ /\ hr)$	Total Engine Weight (kg)	Takeoff Distance (m)	Range (km)
GE9X	3	1,468,000	0.477	28,900	2,680	6,400
Trent 1000-H	4	1,136,000	0.506	23,700	3,600	5,700
Trent 1000-R [13]	4	1,440,000	0.506	24,500	2,740	5,700

The trade studies were conducted with the various propulsion packages using the aircraft sizing from the wing geometry trade study, and the results are given in the table. Mattingly's thrust model was used with an extra correction term, ϵ, introduced into Eq. 20 to match the Mattingly model's TSFC at cruise conditions with the manufacturer claimed TSFC. Thus, the TSFC was computed by

$$TSFC = \epsilon(0.45 + 0.54M_{\infty})\sqrt{\theta}$$

The GE9X's were selected due to their superior fuel economy and reduced weight, with just three engines required to achieve the thrust requirement for the takeoff field length. One major disadvantage, as will be highlighted in the configuration section, is that these engines are much larger than most other turbofan engines, with a radius of approximately 4.1 [14] because of their high bypass ratio of 9.9 and thrust to weight output. This increases drag from having larger engines mounted above the aircraft fuselage, but this was assumed to be a small penalty compared to the fuel consumption savings because the added wetted area is small.

5 Aerodynamics

5.1 Airfoil Selection

Three main considerations guide the selection of an appropriate airfoil. Firstly, the airfoil's design lift coefficient must be determined. An airfoil with a high lift-to-drag ratio and minimal drag at said design lift coefficient is favorable. The critical Mach number of the section must also be considered. Though the aircraft may fly below supersonic speeds, the airfoil accelerates the flow over its surface, creating regions where the local Mach number is greater than that of the freestream. Therefore, an airfoil must be selected such that its local maximum Mach number remains below supersonic to avoid the formation of supersonic shocks in its surface. Lastly, configuration considerations must be given to the selection. A low thickness airfoil is favorable to reduce compressibility and supersonic effects on drag but reduces the available space-claim for internal components. The wing thickness-to-chord ratio is constrained by the maximum fuel volume storage capability, while the payload compartment thickness-to-chord ratio is constrained by the available volume for payloads and passengers.

The airfoil's drag divergence Mach number M_{dd} can be estimated using Korn's relation:

$$M_{dd} = \kappa - \frac{t}{c} - 0.1C_{l_{design}}$$

Where κ is a constant obtained through CFD analysis, and Gudmundsson [6] recommends a value of 0.95 for NASA-style supercritical airfoils. $C_{l_{design}}$ is the airfoil's design lift coefficient. It was initially estimated that the design lift coefficient for Caladrius would lie in the range 0.4-0.6. An initial analysis of the drag divergence of NASA Supercritical airfoils was conducted, and is shown in Table 10:

Table 10: Candidate Airfoils

Airfoil	$C_{l_{design}}$	t/c	M_{dd}
SC(2)-0614	0.6	14%	0.75
SC(2)-0610	0.6	10%	0.79
SC(2)-0606	0.6	6%	0.83
SC(2)-0414	0.4	14%	0.77
SC(2)-0410	0.4	10%	0.81
SC(2)-0406	0.4	6%	0.85

These airfoils were analyzed with the considerations above in mind. The wing fuel volume can be verified in OpenVSP using conformal geometries. These are subgeometries of a major component (wing-body) and, by setting the density of the conformal object to 1, its mass becomes numerically equal to its volume, and the former can be computed within the software.

The design lift coefficient was verified after the comprehensive trade studies. Figure 12 shows the variation in lift coefficient throughout the three design missions:

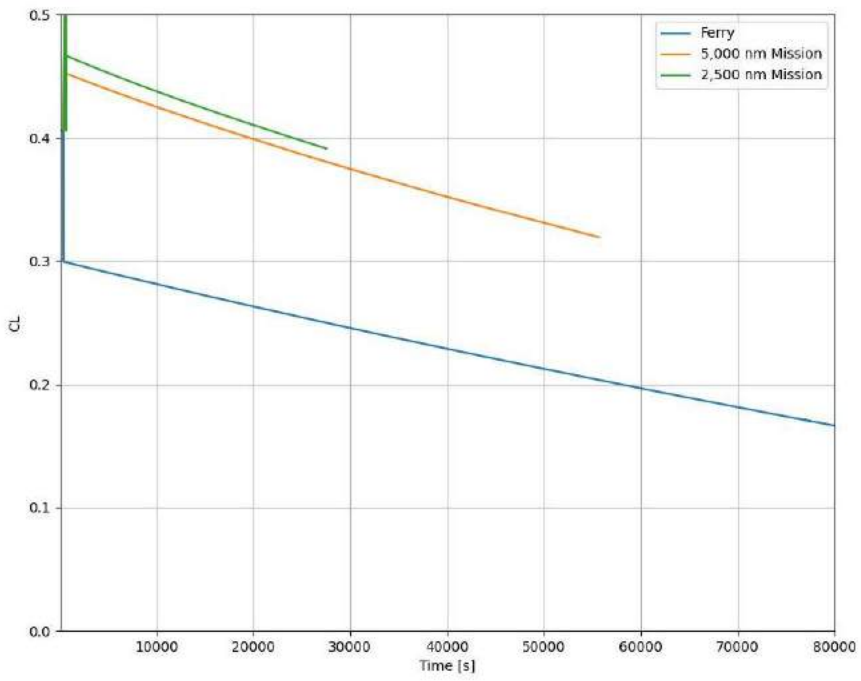

Figure 12: Lift coefficient variation throughout design missions

A target sectional value of 0.4 was selected to closely match the 5,000 nm mission and is not too far from the other design missions of Caladrius. The polars for the candidate airfoils are shown in Figure 13:

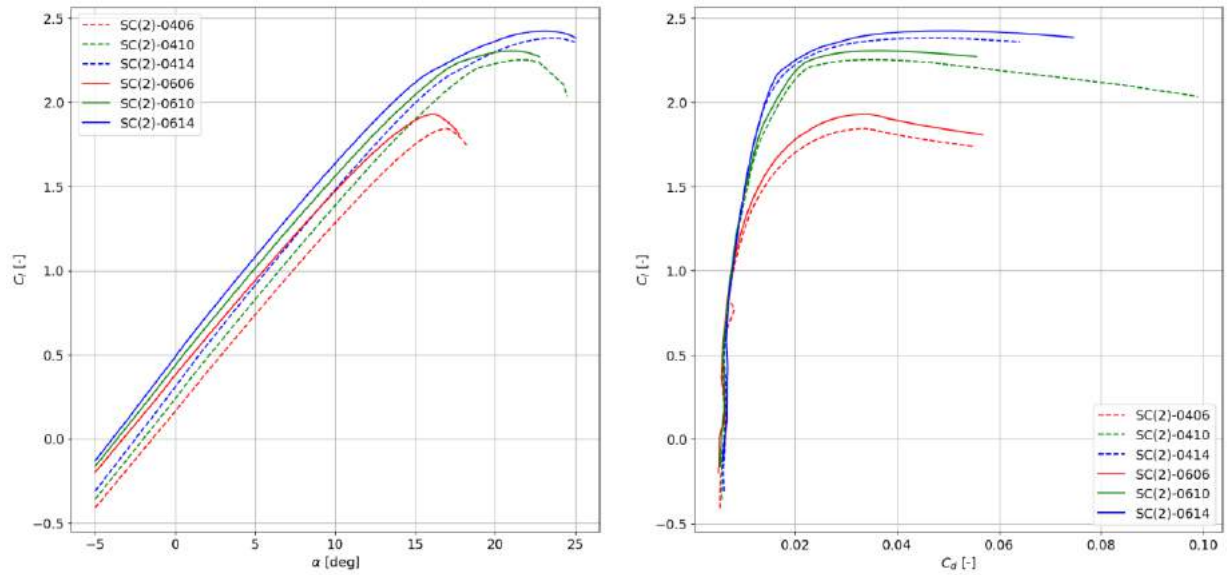

Figure 13: Lift and Drag Polars for Candidate Airfoils

Some conclusions can be made from the polars above. First, there is a sharper drop in $C_{l_{max}}$ from the lower thickness airfoils than among the higher 10% and 14% thickness sections. It was assumed during trade studies that the aircraft is able to attain a $C_{L_{max}}$ of 2 in order to meet takeoff performance requirements. This might not be possible with the thinner supercritical airfoils. This is of particular concern for Caladrius given the low aspect ratio. The lift-curve slope after aspect ratio effects are considered is:

$$a = \frac{a_0}{1 + 57.3\frac{a_0}{\pi e AR}}$$

And is worked out to be only around 70% of the 2D lift-curve slope for the aspect ratio and Oswald efficiency of Caladrius, so an airfoil with zero angle-of-attack lift-coefficient of 0.4 that attains its maximum lift coefficient of 1.6 at 15 degrees will only obtain a lift coefficient of around 1.2 at the same angle of attack. These numbers are representative of low-thickness supercritical airfoils as shown in Figure X. This indicates that a higher thickness is favorable for takeoff performance.

The drag difference among the airfoils at the design lift coefficient is negligible: around 10 counts. Furthermore, 6% thickness supercritical airfoils were not able to meet the fuel volume requirements as verified using conformal geometries in OpenVSP [18]. The decision was made to select the high-thickness, SC(2)-0414 for the wing. The obvious downside is the potential drag divergence at cruise conditions. However, high-thickness airfoils were simulated in the time-based code, and no drag-divergence was verified in the compressible model. This is confirmed by the sensitivity studies conducted and presented in Figure X. However, this selection warrants further investigation with empirical and higher-fidelity numerical methods.

The airfoil selection for the fuselage offers more significant configuration constraints. The placement of 3 main battle tanks (MBTs) as well as large passenger and paratrooper decks creates large internal volume requirements. The aft section of the wing-body fuselage must be wide enough to carry the required payload at the desired longitudinal location to achieve the static margins designed for. This puts the NASA supercritical airfoils at a disadvantage: the trailing-edge cusp takes away a significant amount of available cross-sectional area.

For this purpose, a family of airfoils was designed in XFOIL [19]. The NASA SC(2)-0414 was used as a baseline, and changes were slowly made to both its geometry (direct design) as well as desired pressure coefficient (inverse design) to arrive at potential sections that compromised lift and drag characteristics for gained internal volume by an increase in cross-sectional area. The superposed airfoils as well as their resulting polars with the SC(2)-0414 as a comparison are shown in Figure 14:

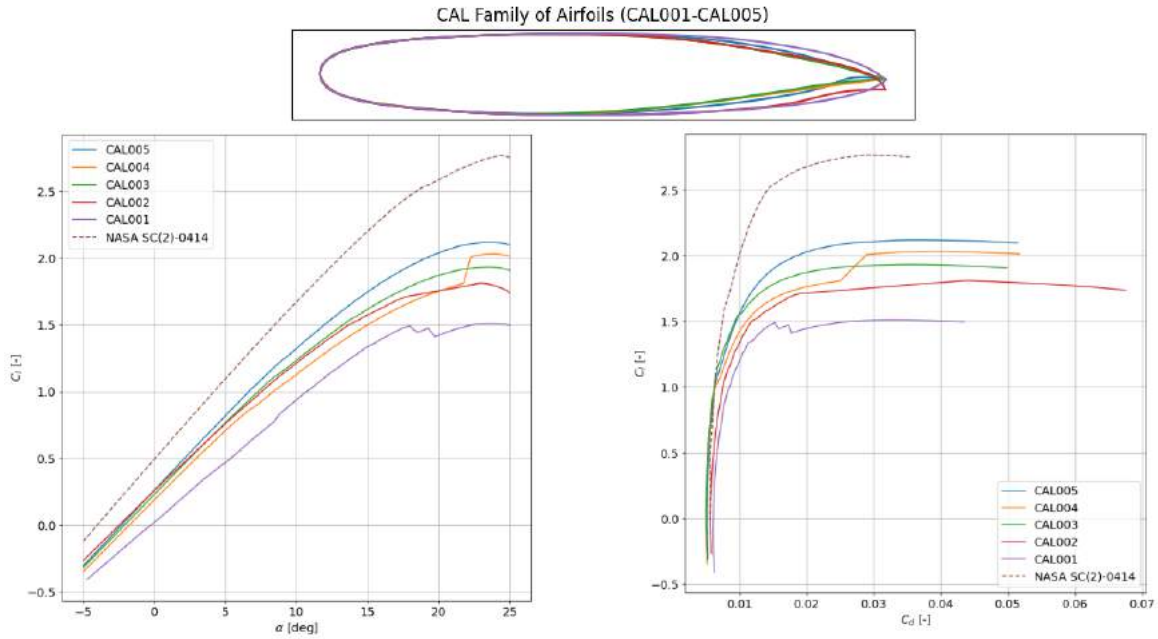

Figure 14: Lift and Drag Polars for CAL family of airfoils

A good compromise was achieved with the design of CAL005. Its maximum sectional lift coefficient remained above the target $C_{l_{max}}$ of 2.0. Additionally, the airfoil's drag coefficient at the design lift-coefficient is slightly lower – by around 3 counts of drag – than that of the baseline SC(2)-0414. The airfoil was designed as to maintain the leading edge geometry of the SC(2)-0414, which is of importance in the pressure drop region of the C_p plot, and effort was made to maintain the rooftop distribution characteristic of the supercritical family of airfoils. Figure 15 shows the CAL005 superposed to the SC(2)-0414 and a zoomed in drag polar:

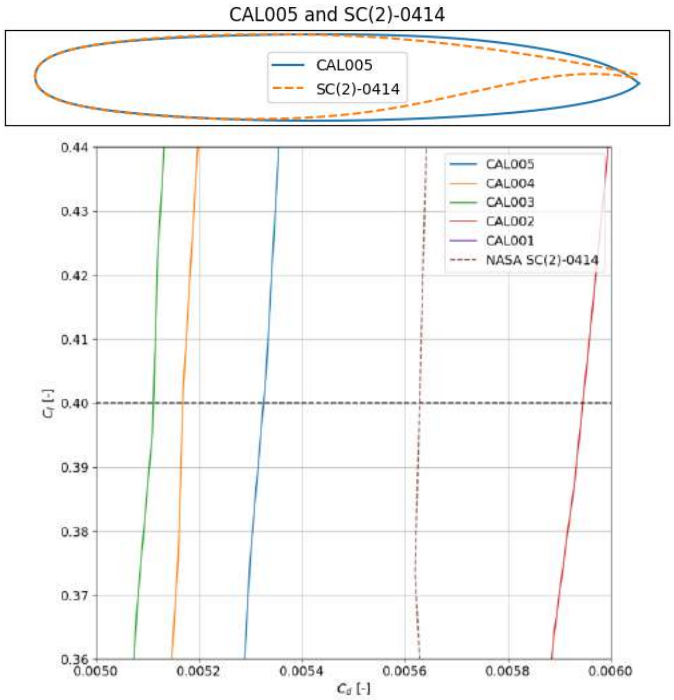

Figure 15: CAL005 Geometry and Polar

And the airfoil was verified to fit all required payloads and passengers in a preliminary OpenVSP model:

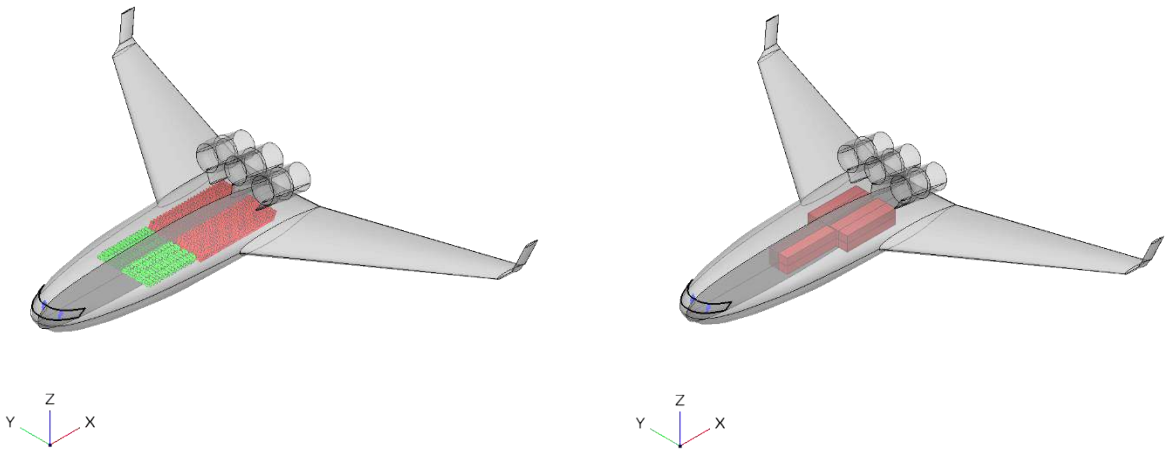

Figure 16: Preliminary CAL005/SC(2)-0414 Configuration Layout

5.2 High Lift Devices: DATCOM Analysis

During trade studies, it was established that a target maximum 3D lift coefficient of 2.0 was required to achieve takeoff performance requirements. The DATCOM [17] provides an analytical method to calculate the 3D maximum lift-coefficient $C_{L_{max}}$ as a function of Mach number with corrections for sweep and airfoil shape. The method uses the airfoil sharpness parameter, Δy, shown in Figure 17:

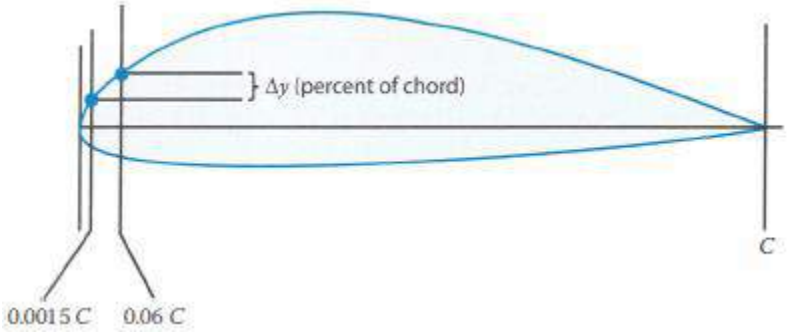

Figure 17: DATCOM Airfoil Sharpness Parameter (adapter from Raymer [7])

This is computed for the design airfoil of Caladrius to be 3.5. This is used to find $C_{L_{max}}$ corrections for a given leading-edge sweep.

Per DATCOM, the maximum lift coefficient at a given Mach number is computed as:

$$C_{L_{max}} = C_{l_{max}} \left(\frac{C_{L_{max}}}{C_{l_{max}}} \right) + \Delta C_{L_{max}}$$

. Where the left term is the low-subsonic maximum lift-coefficient and is a function of the sectional maximum lift. The term $\left(\frac{C_{L_{max}}}{C_{l_{max}}}\right)$ is simply the ratio between 3D and 2D maximum lift coefficient and is a function of the sharpness parameter for typical families of airfoils.

The second term, $\Delta C_{L_{max}}$, are the corrections for high-subsonic and transonic speeds. DATCOM only provides values for leading edge sweeps of 20 and 40 degrees, respectively, and does not cover the entire range of Mach numbers desired. Therefore, a logarithmic fit was used to extrapolate values for the corrections as follows:

$$\Delta C_{L_{max,20^\circ}} = -0.352 \log M - 0.5628$$

$$\Delta C_{L_{max,40^\circ}} = -0.191 \log M - 0.2948$$

And a value is interpolated between the curves for Caladrius' leading-edge sweep of 35 degrees. The fits above show good agreement with tabulated DATCOM data. From this, the clean $C_{L_{max}}$ variation with Mach number is found. The increment in maximum lift-coefficient can be accounted for by a simple analytical method:

$$\Delta C_{L_{max,flaps}} = 0.9 \Delta C_{l_{max}} \left(\frac{S_{flapped}}{S_{ref}}\right) \cos \Lambda_{H.L.}$$

Where $\Delta C_{l_{max}}$ is the change in sectional lift coefficient for a given high-lift device, tabulated in Raymer; $S_{flapped}/S_{ref}$ is the flapped area ratio, assumed to be around 66%, and $\cos \Lambda_{H.L.}$ is the cosine of the angle formed by the hinge line of the high-lift devices and a horizontal reference line. This was estimated in OpenVSP using assumed chord fractions.

The variation in clean maximum lift coefficient is plotted in Figure 18 along with a study of potential high-lift devices and their variations:

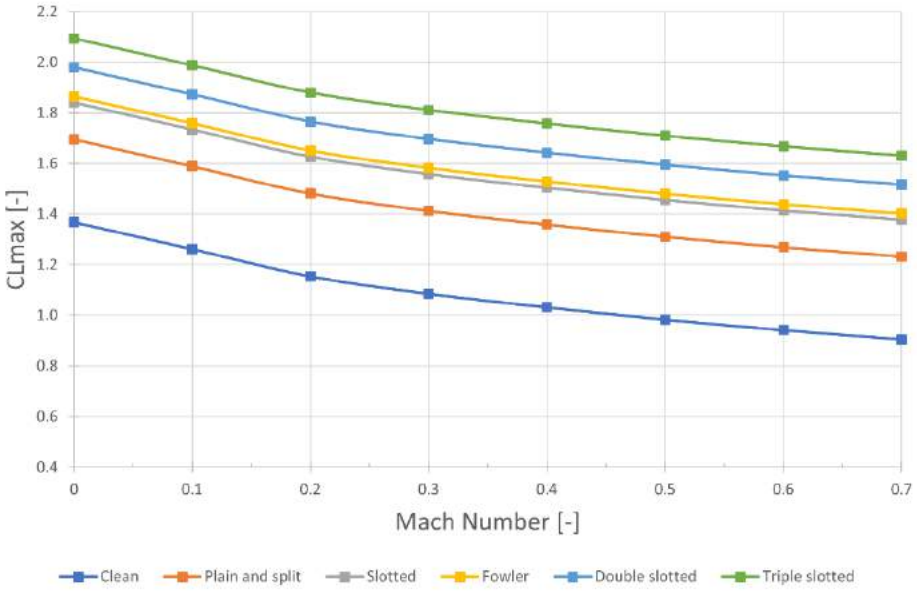

Figure 18: High-Lift Devices Study

Figure 18 indicates the need of, at the very least, a double slotted high-lift device system to achieve the required maximum lift coefficient for takeoff requirements per the wing geometry trade studies.

5.3 Drag Polars

Drag polars for the preliminary design of Caladrius are shown in Figure 19 and Figure 20:

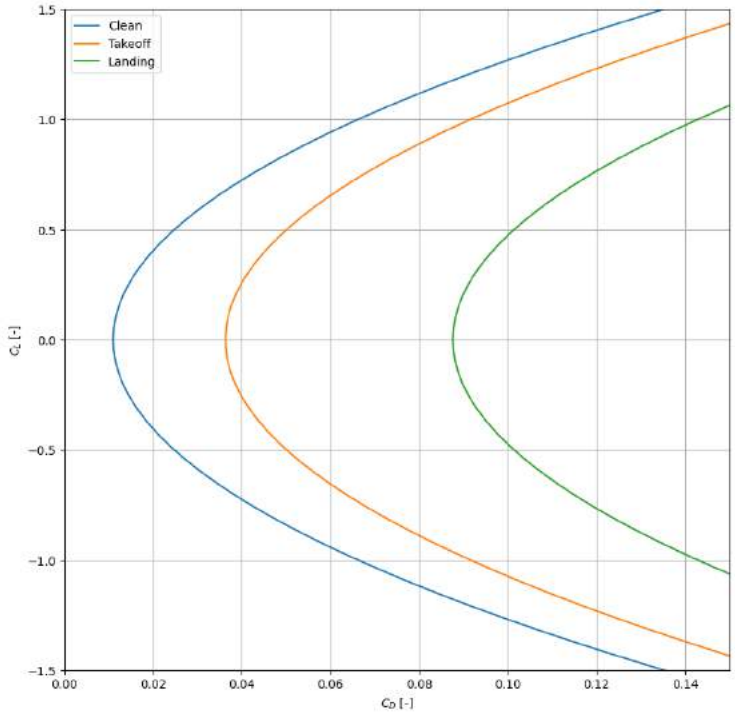

Figure 19: Drag Polars for Clean, Takeoff, and Landing Configurations

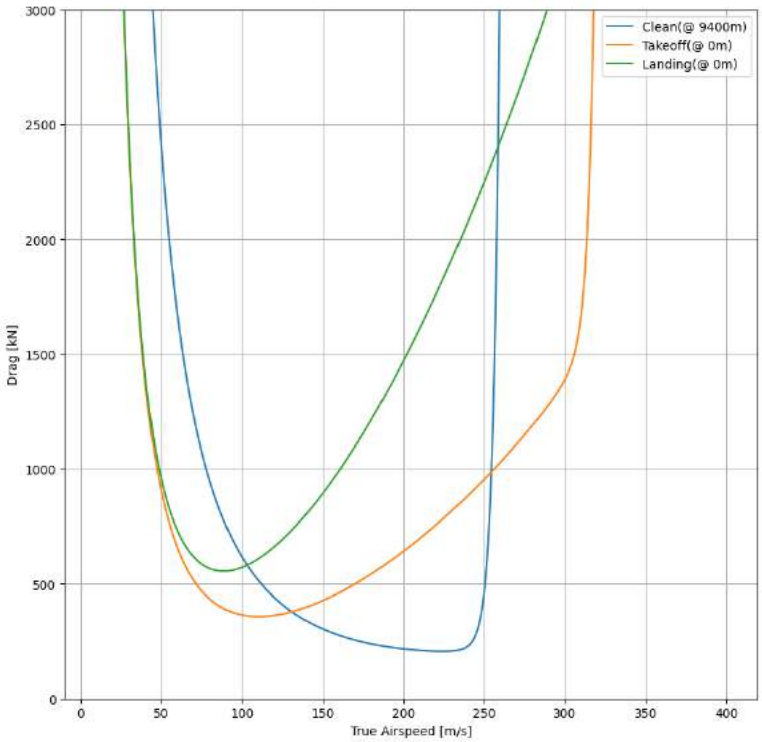

Figure 20: Drag Polars for Clean, Takeoff, and Landing Configurations

The computed drag coefficients for each configuration were computed to be $C_{D,0\ clean} = 0.011$, $C_{D,0\ tko} = 0.036$, and $C_{D,0\ ldg} = 0.088$. For landing, the contribution to parasite drag spoilers were estimated by:

$$c_{d,s} = \frac{1.17 b_s h_s}{S}\left(\frac{\Delta S}{90}\right)$$

where b_s is the span of the spoilers, h_s is the height of the deployed spoiler, and ΔS is the deployment angle of the spoilers.

It should be noted that the clean parasite drag coefficient does vary during flight because of the lift coefficient changes with aircraft weight changes, effecting the compressible drag correction. This means that the parasite drag coefficient tends to decrease during flight, as shown in Figure 21:

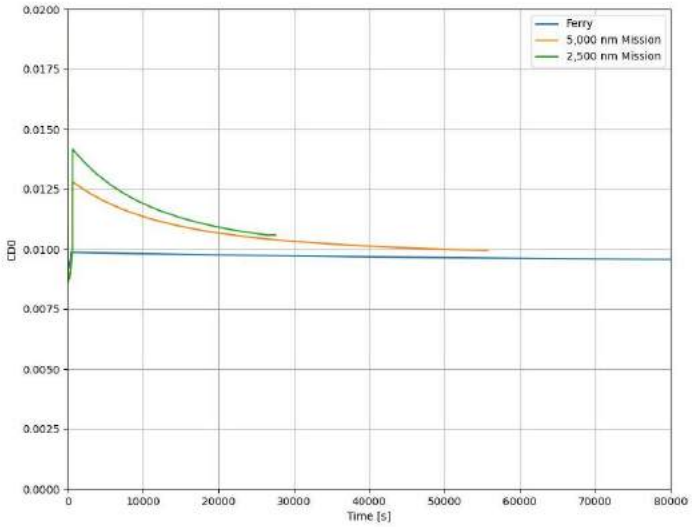

Figure 21: Variation in Parasite Drag with Time

5.4 Stability & Control

The goal of stability is to ensure the aircraft can correct any disturbances and return to its original state to maintain its attitude in flight. This chapter deals with the design and analysis for static longitudinal and directional stability. For static longitudinal stability, the aircraft must have $\partial \boldsymbol{C_M}/\partial \alpha < 0$**.** This is achieved by placing the center of gravity forward of the neutral point. To determine the neutral point location, two source-vortex panel models were created in AVL [15] and XFLR5 [16], shown in Figure 22:

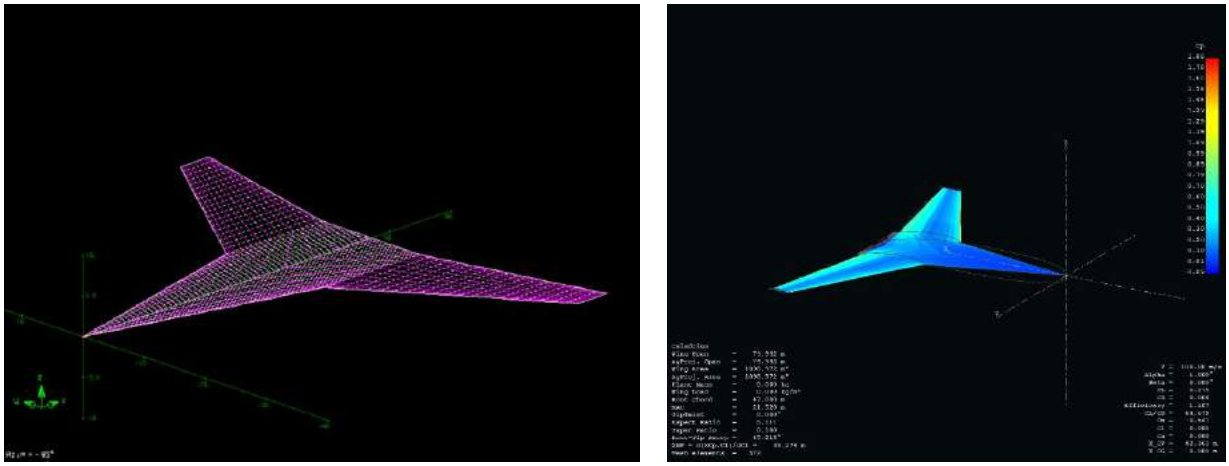

Figure 22: AVL (left) and XFLR5 (right) Source-Vortex Panel Models

From these models, the neutral point is determined to be 37.4m from the nose of Caladrius. Aircraft of similar weight category typically have an SM of 8%-30% (Gudmundson) and except for the initial ferry mission, which was sized to 37.5% less than the lower bound for static margin, every other mission will fly at this range of static margin. The ferry mission is also balanced so that the center of gravity eventually falls within the envelope from the shift in weight from fuel burn.

Directional stability is achieved when $C_n = 0$ with no sideslip angle, and $\partial C_n/\partial\beta > 0$. Caladrius attains directional stability by the presence of vertical surfaces at the wingtips (winglets.) Finally, roll stability is achieved through the dihedral effect, $\partial \boldsymbol{C_l}/\partial\beta$. The derivative must be negative, and can be obtained through the use of dihedral as well as planform design.

The blended wing design deviates from the traditional horizontal and vertical tail configuration. Thus, without the standard elevators and ailerons to control pitch and roll, respectively, elevons had to be incorporated. Elevons can control the pitch and roll of the aircraft. When the two elevons are activated in the same direction, a pitching moment is created that moves the nose of the plane upwards or downwards, and when each elevon is activated in different directions, a rolling positive moment is generated towards the elevon that is upwards. These control surfaces are placed at the trailing edge of the wings.

Caladrius meets static stability requirements for all missions. Sample result from AVL [15] is shown in Table 12:

Table 12: Stability Derivatives (SM = 8%)

Stability Derivative	C_{m_α}	C_{l_β}	C_{n_β}
Requirement	Negative	Negative	Positive
Result	-0.535	-0.05	0.0023
Meets Requirement?	YES	YES	YES

6 Aircraft Sizing

The table below shows the proposed aircraft's sizing from the propulsion and aerodynamic studies.

Table 13: Final Aircraft Sizing from Trade Studies

Parameter	Variable	Dimension
Fuselage Length	l_{fus}	46 m
Fuselage Diameter	d_{fus}	10 m
Airfoils	[-]	CAL005 (Fuselage) SC(2)-0414 (Wing)
Wing Span	b	65 m
Wing MAC	$\bar{c}$	10.1 m
Wing Area	S	659 m^2
Aspect Ratio	AR	6.4
Taper Ratio	λ	0.3
Sweep	Λ	35 deg.
Parasitic Drag Coefficient	$C_{D,0}$	0.011

Parasite Area of Fuselage	A_{fuse}	3.5 m^2
Parasite Area of Plane	A_{plane}	6.1 m^2
Stall Velocity	V_{stall}	70.4 m/s
Maximum Lift to Drag Ratio	E_{max}	21
Cruise Velocity	V_{cruise}	240 m/s (Mach 0.8)
Maximum Lift Coefficient	$C_{L_{max}}$	2.0
Mean Chord Reynold's Number	Re_c	$68 \cdot 10^6$
Cruise Drag	D_{cruise}	190 kN
Minimum Drag	D_{min}	180 kN
Velocity at D_{min}	$V_{D_{min}}$	145 m/s
Minimum Power Required	$P_{R,min}$	32 MW
Velocity at $P_{R,min}$	$V_{P_{min}}$	110 m/s
Empty Weight	W_{empty}	141,000 kg
Maximum Fuel Load	W_{fuel}	123,600 kg
Maximum Takeoff Weight	**MTOW**	407,000 kg
Maximum Landing Weight	**MLOW**	355,000 kg

Note: All performance values dependent on the aircraft weight are given at MTOW in the table above

7 Aircraft Performance

7.1 Performance Summary

The table below lists the proposed aircraft's performance for each of the three missions.

Table 14: Mission-Specific Performance Values

	430,000-lb Payload Mission	295,000-lb Payload Mission	Ferry Mission
Parameter	**407,000 kg Gross Weight (195,000 kg Payload)**	**400,000 kg Gross Weight (133,800 kg Payload)**	**270,000 kg Gross Weight (No Payload)**

Total Takeoff Distance*	2,680 m (8,800 ft)	2,560 m (8,400 ft)	1,080 m (3,500 ft)
Total Landing Distance*	2,490 m (8,200 ft)	2,340 m (7,700 ft)	1,650 m (5,400 ft)
High-speed Cruise Range (Mach 0.8)**	6,050 km (3,260 nm)	12,700 km (6,850 nm)^	21,600 km (11,700 nm)^
Maximum Range **	6,400 km (3,460 nm) at Mach 0.78	13,500 km (7,290 nm) at Mach 0.77^	21,900 km (11,800 nm)^
Maximum Endurance**	8.0 hrs at Mach 0.70	17.2 hrs at Mach 0.67^	28.0 hrs at Mach 0.64^
Maximum Climb Rate (Sea Level)	24 m/s (4,700 fpm)	24 m/s (4,700 fpm)	44 m/s (8,600 fpm)
Maximum Climb Rate (3000 m)	22 m/s (4,300 fpm)	22 m/s (4,300 fpm)	38 m/s (7,500 fpm)
Minimum Turning Radius (Sea Level)	600 m (2,000 ft)	600 m (2,000 ft)	350 m (1,100 ft)

* At ISA+15℃ conditions at sea level.
** With 45-minute fuel reserves.
^ Assuming step climb at constant mach.

Table 15 gives the aircraft V-speeds at various gross weight configurations. Note that these weights do not necessarily correspond to any mission because the 2,500 nm and 5,000 nm missions have similar takeoff weights.

Table 15: V-speeds at Various Gross Weight Configurations

Speed	407,000 kg Gross Weight	310,000 kg Gross Weight	213,000 kg Gross Weight
V_1	71.3 m/s (138 KIAS)	58.4 m/s (113 KIAS)	43.7 m/s (85 KIAS)
V_{stall}	70.4 m/s (137 KIAS)	61.4 m/s (119 KIAS)	50.9 m/s (99 KIAS)
V_r	80.9 m/s (157 KIAS)	70.6 m/s (137 KIAS)	58.5 m/s (114 KIAS)
V_y *	164 m/s (320 KIAS)		
V_x *	122.4 m/s (238 KIAS)	102 m/s (198 KIAS)	78.3 m/s (152 KIAS)
V_a	121.9 m/s (235 KIAS)	106.3 m/s (206 KIAS)	88.1 m/s (171 KIAS)
V_{mo}	164 m/s (320 KIAS)		
M_{mo}	0.82		
V_{ref}	90.6 m/s (178 KIAS)**	79.8 m/s (155 KIAS)	66.1 m/s (128 KIAS)

Note: All airspeeds in m/s are true airspeed at sea level, standard atmospheric conditions.
* At sea-level, ISA conditions ** Over maximum landing weight

The flight envelope, shown below, incorporates stall, thrust available, and design maximum airspeed limitations, showing the velocity range at various airspeeds. Note that a service ceiling of 43,000 ft was designed to for structural limitations with pressurization. Figure 23 shows that at lower weights, the aircraft theoretically has enough thrust to cruise at altitudes over 43,000 ft, but these are not considered part of the flight envelope.

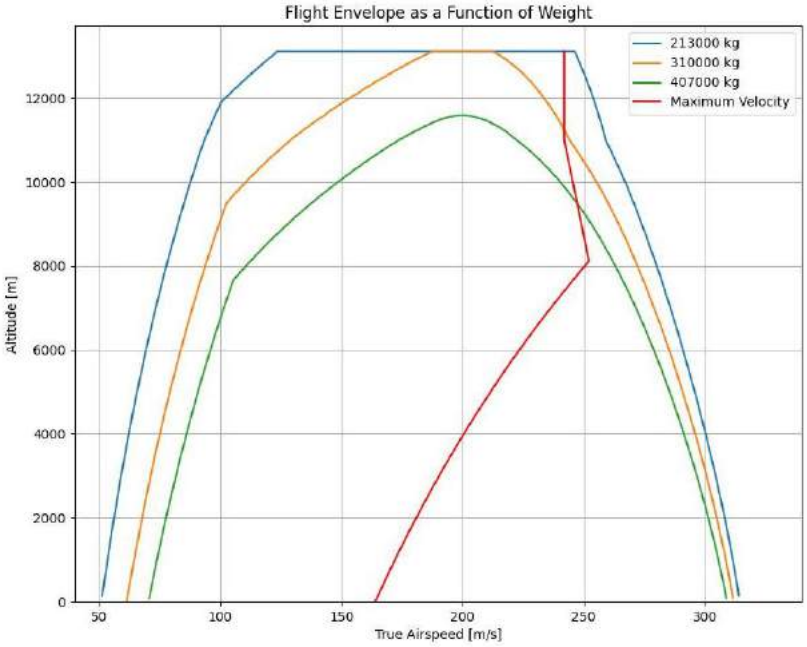

Figure 23: Flight Envelope as a Function of Weight

7.2 Payload Range

The maximum range at a high-speed Mach 0.8 cruise with 45-minute reserves is plotted as a function of payload assuming the maximum permissible fuel load is loaded. An economic step-climb model was used for these computations. The graph has two distinct regions: from no payload to approximately 1.4 MN of payload (140,000 kg) and from 1.4 MN of payload to maximum payload at MTOW. In the first region, the aircraft is below its maximum gross weight at takeoff and can take its full fuel load of 123,600 kg, so differences in range in this region are due to differences in drag from aircraft weight. Above a 140,000 kg payload, the aircraft is weight limited and cannot take full fuel; therefore, the range decreases more quickly with higher payload weights and range is more fuel limited.

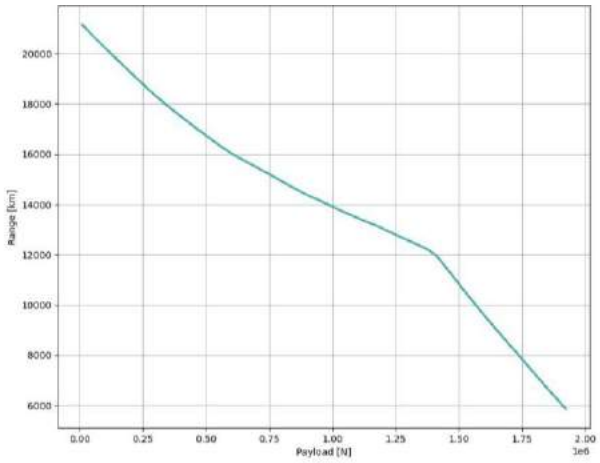

Figure 24: Aircraft Range as a Function of Payload Weight

7.3 Rate of Climb

The RoC is given in the figures below as a function of payload weight and altitude. At maximum gross weight, the aircraft has an absolute ceiling of approximately 11,000 m (36,000 ft) with a maximum climb rate at sea level of 24 m/s (4,700 fpm). All RoC graphs implement minimum and maximum velocity limits; minimum velocity limit is set by the stall speed at the given altitude, while the maximum velocity is set as the minimum of the maximum Mach velocity (0.82) or the maximum indicated airspeed (320 KIAS, or 164 m/s). In the minimum weight configuration, the aircraft has a ceiling of 13,300 m (43,000 ft), complying with mission requirements. At most airspeeds, the aircraft RoC is not performance limited, but rather structurally limited; in other words, the aircraft cannot achieve its theoretical best rate of climb speed at most altitudes (other than near its service ceiling) because it is greater than the aircraft's never exceed speed (V_{ne}).

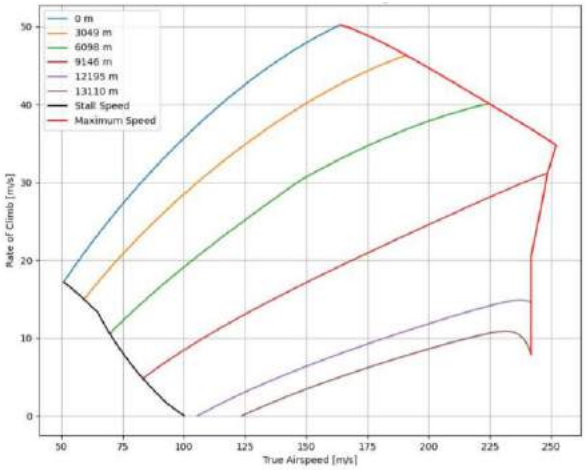

Figure 25: Aircraft RoC at MTOW

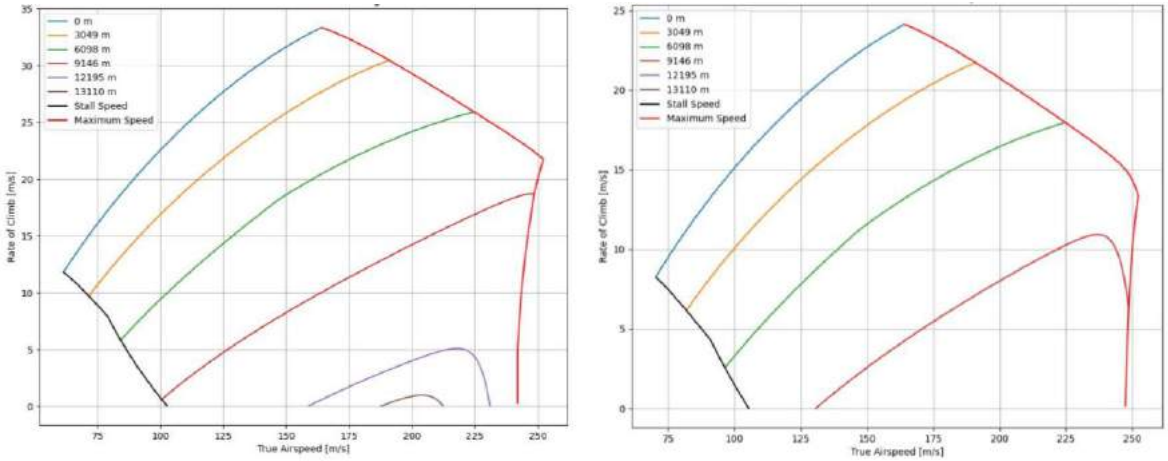

Figure 26: Aircraft RoC at 310,000 kg Gross Weight (left) and 213,000 kg Gross Weight (right)

The RoC charts were limited by the maximum and minimum airspeeds of the aircraft, defined respectively as the stall speed (black line) and the minimum of V_{mo} or M_{mo} at a given altitude (red line). At lower altitudes, V_{mo} is the limit on the maximum airspeed, while the maximum Mach number limits the flight envelope at higher altitudes.

7.4 Takeoff Performance

Short-field takeoff performance (assuming a static takeoff) computed by the time-based takeoff model is plotted as a function of takeoff weight and density altitude (at 300 m, or 1,000 ft, increments from sea level). At sea level in ISA+15℃ conditions, the aircraft has a takeoff field length per 14 CFR § 25.111 of 2,680 m (8,800 ft). At density altitudes of 2,400 m (8,000ft), the minimum runway field length is in excess of 3,500 m (11,400 ft), so the aircraft will have limited high-density altitude performance and will be primarily limited to near sea-level airfields. The quadratic dependence of takeoff distance on weight is consistent with simpler analytical models and highlights how constraining takeoff performance is to this HLA aircraft design.

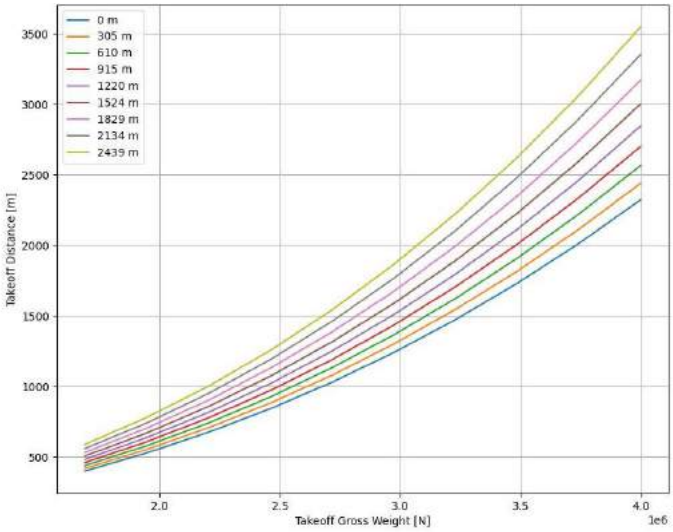

Figure 27: Aircraft BFL as a function of Gross Weight and Density Altitude

7.5 Landing Performance

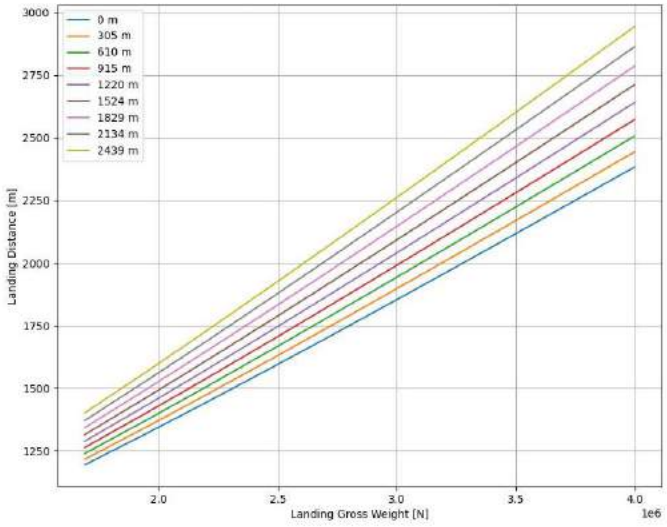

Figure 28: Aircraft BFL as a function of Gross Weight and Density Altitude

Landing performance computed by the time-based landing model is plotted as a function of gross weight and density altitude (at 300 m, or 1,000 ft, increments from sea level). At sea level in ISA+15℃ conditions, the aircraft has a landing field length per 14 CFR § 25.125 of 2,200 m (7,200 ft) at its maximum landing weight of 355,000 kg. The maximum landing weight was selected to limit the aircraft's V_{ref} to 165 KIAS (84.9 m/s) to certify the aircraft for the Category D approach category under 14 CFR § 97.3. Unlike takeoff performance, there is less of a quadratic dependence on weight; this is because regardless of aircraft weight, a constant descent angle is assumed. This means that the airborne distance of the overall landing distance does not vary quadratically with weight. Furthermore, because the coefficient of friction is assumed to be constant, at higher weights, the aircraft can produce more friction during rollout, decelerating more quickly. Thus, a more linear dependence of landing distance with weight is observed in Figure 28.

7.6 Turning Performance

The turning performance as a function of weight and dynamic pressure for the designed aircraft is shown below. Aerodynamic, structural, and propulsive turning constraints are implemented by Eq. 21-23.

$$r_{C_{L_{max}}} = \frac{2\left(\frac{W}{S}\right)}{\rho g\left(\left(C_{L_{max}}q\right)^2 - \left(\frac{W}{S}\right)^2\right)^{1/2}}q \tag{21}$$

$$r_{struct} = \frac{2}{\rho g\sqrt{n_{struct}^2 - 1}}q \tag{22}$$

$$r_{thrust} = \frac{2}{\rho g\sqrt{(\frac{qS}{kW^2})(T_A - C_{D,0}qS) - 1}}q \tag{23}$$

Results indicate that, especially in a heavy configuration, the aircraft's turn performance is limited primarily by thrust limitations due to significant increases in induced drag at high load factors. At sea-level, the aircraft at MTOW has a minimum turning radius of approximately 600 m (2,000 ft), found as the intersection of the thrust and $C_{L_{max}}$ limit curves at a dynamic pressure of approximately 6,000 Pa. At a cruising altitude of approximately 11,000 m, the turning performance at heavy gross weights is entirely limited by thrust limitations because the aircraft is near its service ceiling.

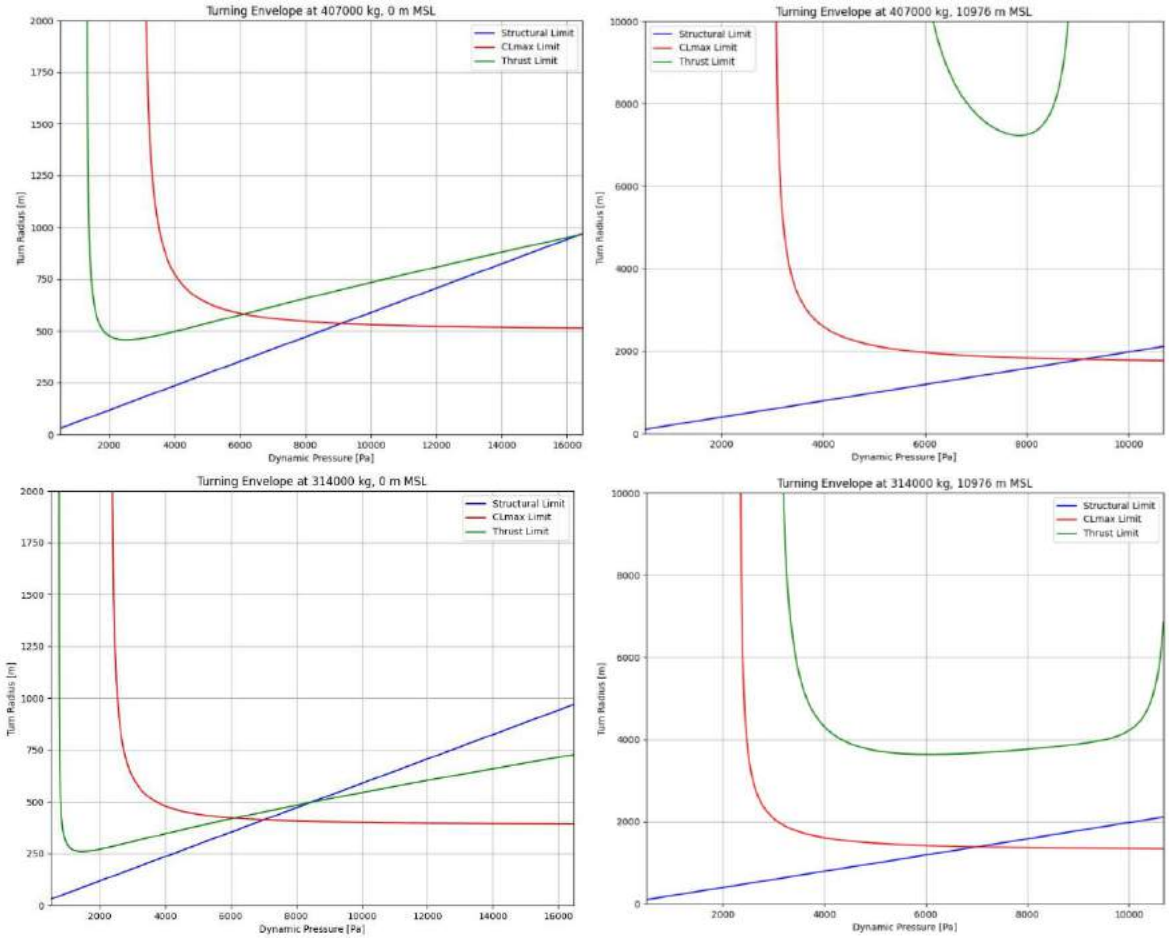

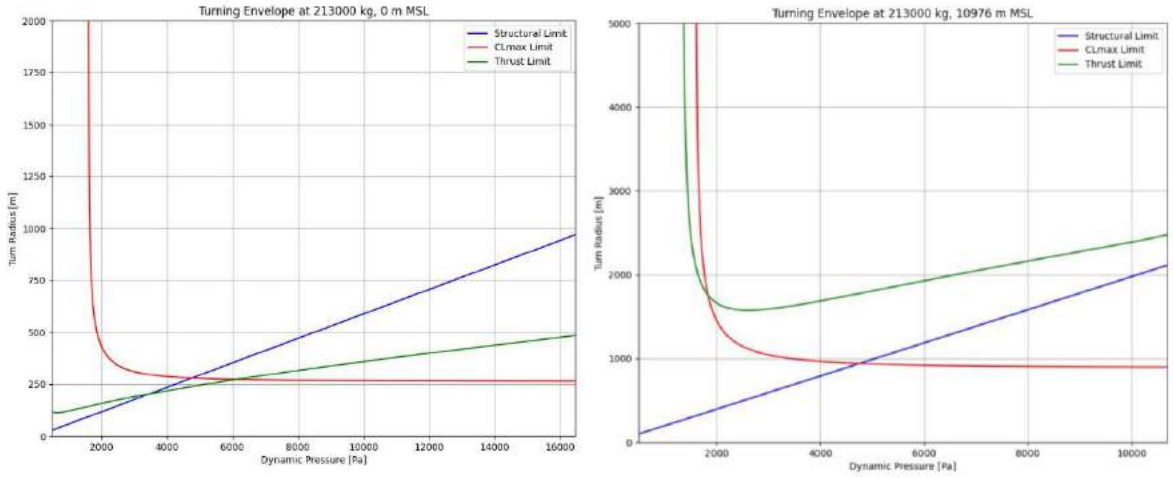

Figure 29: Turning Performance as a Function of Weight and Dynamic Pressure

7.7 V-N Diagram

A flight envelope diagram shown in Figure 30 was constructed assuming a positive g-load limit of +3 g's and a negative g-load limit of -1.5 g's. The maximum airspeed is set as the design V_{ne}. At MTOW, the aircraft has a maneuvering speed (the maximum airspeed at which the aircraft will stall before exceeding its maximum design load factor) of approximately 121.9 m/s (235 KIAS).

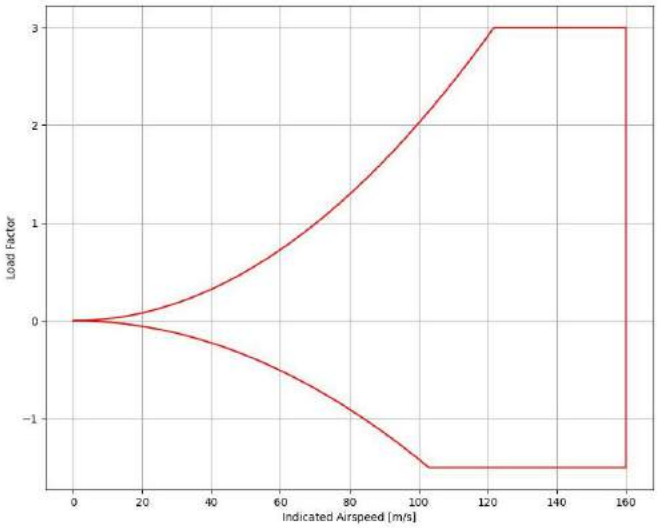

Figure 30: Aircraft V-n Diagram at MTOW

8 Aircraft Configuration

The following section outlines details of the aircraft subsystems, including gear location and sizing, engine placement, fuel systems, power systems, air systems, hydraulic systems, life support and emergency systems, payload layout, aircraft access, cockpit layout, and onboard avionics and instrumentation.

8.1 Gear Placement

Landing gear locations as seen in table 16 were determined by iterating wheelbase distances until an aftmost and forwardmost nose gear location was found that met guiding values suggested by Raymer [7], included in the table below.

Table 16: Wheelbase distances with respect to aftmost (a) and forwardmost (f) centers of gravity

Parameter	Distance [m]
Wheelbase, B	24.1
N_a	22.3
N_f	20.7
M_a	1.77
M_f	3.40

Table 17 shows the required and preferred values set by Raymer [7] and the respective values for the current aircraft landing gear placement. The preferred values could not exactly be met as this would cause the aircraft to become statically unstable on takeoff during the ferry mission.

Table 17: Gear Placement Criteria

Criteria	Requirement	Preferred	Caladrius
$\frac{M_a}{B}$	> 0.050	0.08	0.0734
$\frac{M_f}{B}$	< 0.200	0.15	0.141

A fuselage height off the ground of 2 meters was chosen which yields a maximum rotation angle of 17.4 degrees on takeoff.

8.2 Wheel Layout and Sizing

Wheel layout for Caladrius was chosen based on an assigned max Aircraft Classification Number (CAN) of 55 with the corresponding Pavement Classification Number (PCN) on flexible pavement with subgrade B. The PCN is set per airport based on their respected taxiways and the ACN is set from the design and location of loads projected on the taxiway for each aircraft. To achieve a max ACN of 55 for the listed requirements, Caladrius will feature a layout very similar to the Airbus A-380. This layout features two nose tires at the nose gear and twenty main landing gear tires. Viewing the A-380 Manual [20] PCN tables, it was found that at a weight variant of WV013 and aircraft mass of 494,000 kg, the ACN is 55 with each tire inflated to 203 psi. As the Caladrius MTOW is 407,000 (120% less than that projected for the A-380 CAN), the assumption of using A-380 landing gear layout is confirmed to meet the requirements.

Wheel sizing was confirmed using the theory from Raymer [7] stating that the main tires carry 90% and nose wheels carry 10% of the aircraft weight. Assuming the A-380 landing gear layout, the Goodyear Flight Leader 498F29-3 [21] is the most optimized tire for the aircraft. Each tire is capable of holding 51639.28 kg and is dimensioned at a 49 inch diameter and 17 inch width per tire. These tires were assumed to be inflated to 210 psi and confirmed 30% FOS with the equation from Raymer [7] for the wheel weight accounting for a rolling radius of 2/3 the tire radius.

8.3 Engine Placement

Three GE9x engines are placed in a symmetrically staggered formation on the top of the blended fuselage with the center engine placed aftmost numbered engines 1, 2, 3 from left to right. The engines were placed on the upper surface of the fuselage to mitigate ground clearance issues as the blended wing body provides minimal ground clearance near the wing root. Additionally, this placement allows increased options for paratrooper deployment. Engines 1 and 3 are shifted forward to mitigate balancing issues. Although the forward placement of engines 1 and 3 near the main body of the fuselage would raise internal noise concerns, these were neglected as the primary mission of the aircraft is military cargo transport.

8.4 Fuel Systems

Two wing tanks and a center tank provide the necessary fuel volume for the aircraft. Wing tanks were sized by offsetting the wing planform to provide necessary room for leading edge and trailing edge wing devices. The area was then multiplied by an average interior thickness of the wing. Tank volumes are specified below in Table 18.

Table 18: Aircraft Fuel Tank Specification

Tank	Volume [L]	Capacity [kg]	% Total Volume
Left	53660	43148	35%
Right	53660	43148	35%
Center	46780	37611	30%
Total	154100	123907	100%

The aircraft is equipped with scavenge pumps and a center bulkhead separating the center fuel tank from the main fuselage structure, complying with all regulations set forth by 14 CFR § 25.951-81. The aircraft is to utilize fuel in the center tanks before the left and right tanks for fire risk mitigation.

The aircraft is also equipped with in-flight refueling infrastructure. A USAF flying boom type receptable is located above the cockpit section and ducts fuel into the center fuel tanks.

8.5 Power Systems

A Pratt and Whitney PW980 gas-turbine auxiliary power unit (APU) will provide bleed air and electrical power for ground operations and engine start. The APU, inlet, and exhaust are located forward of the payload compartment, protected by a firewall complying with 14 CFR § 25.1121. APU fuel will be pumped from the left tank only to reduce fuel line weight. Once started, the three GE9x will provide electrical power and bleed air for electrical and bleed systems on the aircraft such that the APU can be shut down.

8.6 Air Systems

The aircraft bleed air system is shown below in figure 31. Bleed air is supplied by three GE9X and a PW980 APU during no engine operations. Bleed air is ducted throughout the aircraft to provide pressure for the engine starter, anti-ice systems (including but not limited to pitot heat, cowling, static port heat), hydraulic system reservoirs, pressurization systems, and air conditioning systems. The aircraft is equipped with two pressurization air conditioning kits (PACKs) located forward of the payload segment of the fuselage. Two recirculation fans assist payload bay air conditioning to reduce bleed air usage and reduce fuel consumption. These conditioned air sources are mixed in a mixing manifold, which then diverts the conditioned air throughout the cabin. The flight deck air is also sourced directly from the left PACK. Ground air and ground pneumatic air can be provided to the aircraft for ground operations. Water pressure is also provided by bleed systems, although not shown in the figure below.

8.7 Hydraulics Systems

Hydraulic power is supplied by three hydraulic reservoirs distributed through the aircraft in addition to a standby reservoir. The left and right hydraulic systems are powered by a primary pump supplied by engine power and standby electric pumps during unexpected periods of high demand emergencies. Hydraulic pressure is provided by the bleed system. The center hydraulic system is primarily powered by an electric pump but includes two bleed powered air pumps and a standby electric pump for redundancy. The standby reservoir system is powered by a single electric pump. Hydraulic systems are interconnected to provide redundancy in case of failure; however, the left and right hydraulic reservoirs are primarily responsible for the left and right-wing hydraulic systems, while the center reservoir is primarily responsible for fuselage hydraulic systems. Two separate power transfer units (PTU) allow hydraulic power transfer in case of a system emergency. Figure 32 outlines a high-level overview of the aircraft's hydraulic system. A Ram Air Turbine (RAT) is included in the center reservoir system in case of complete hydraulic power failure. The nose and main gear systems are on isolated branches to allow a manual gear drop. All control surfaces, landing gear, main cargo doors, brakes, spoilers, and thrust reversers are actuated by hydraulic systems.

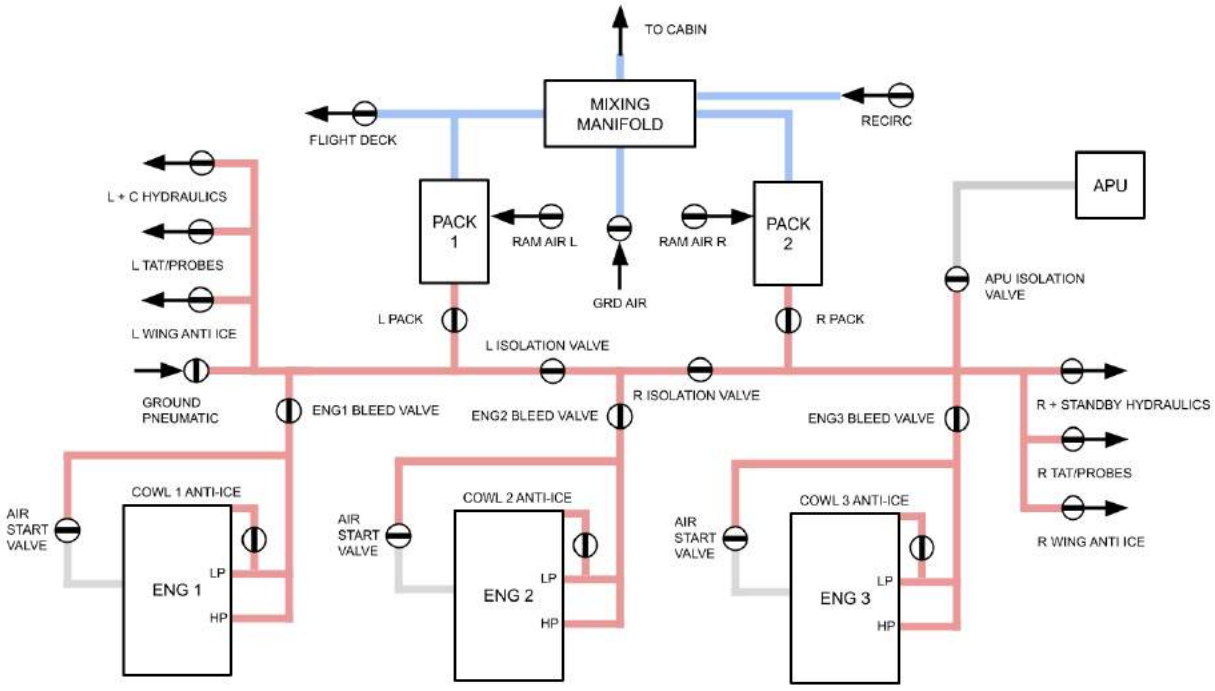

Figure 31 Error! No text of specified style in document.**:** Caladrius Bleed Air System Overview

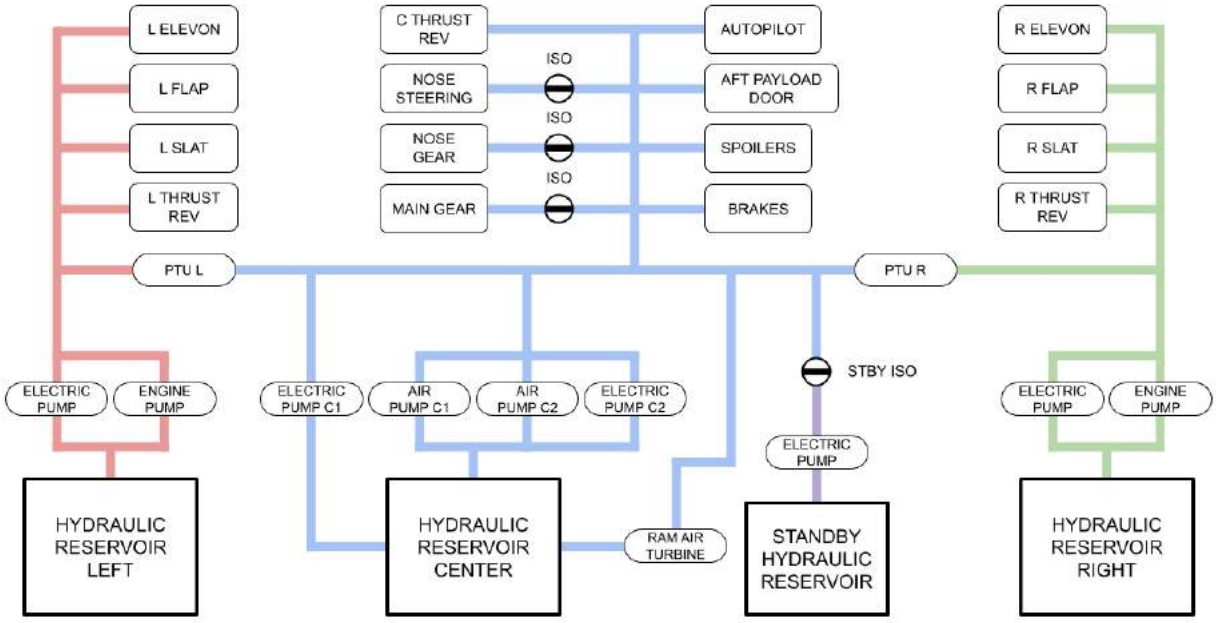

Figure 32Error! No text of specified style in document.: Caladrius Hydraulic System Overview

8.8 Life Support and Emergency Systems

Passenger emergency egress systems are included in the aircraft during passenger transport. Crew emergency egress can be conducted through cockpit windows. Passenger emergency egress can be conducted through jump doors and emergency hatches throughout the main cabin. Passenger emergency egress equipment is stored in 4 equidistant sections along the payload compartment as specified in 14 CFR § 25.1411. To meet 14 CFR § 25.807, five Type I exits are equidistantly placed on each side of the fuselage for a total of 10 emergency exits to support the maximum passenger capacity of 441 passengers.

Supplemental emergency oxygen is provided via two chemical oxygen generators located in the forward payload compartment and the aft payload compartment. These generators provide supplemental oxygen at the amount and rate specified by 14 CFR § 25.1441. A cockpit voice recorder (CVR) and flight data recorder (FDR) are installed in the aft payload compartment to minimize destruction via crash impact heat from a fire and meet CVR-FDR requirements set by 14 CFR § 25.1457-1459.

8.9 Payload Layout

The aircraft supports three main payload configurations for flight. This includes an armored vehicle transport configuration, cargo (pallet) configuration, and passenger/paratrooper transport configuration.

8.9.1 Armored Vehicle Transport

The aircraft can accommodate up to three M1A2 Abrams main battle tanks, each weighing 64600 kg. For balancing, tanks will be loaded two abreast, biasing the mass towards the aft of the aircraft. This ensures a minimal change of the static margin during flight. Tanks will be loaded through the aft cargo door.

Figure 33 Error! No text of specified style in document.**:** Tank Payload Configuration

8.9.2 Cargo Pallet Transport

A maximum of 48 463L master pallets (HCU-6/E) can be loaded in the main payload bay with a total payload weight of 188000kg. This payload layout takes up the entire payload bay footprint. Payloads will be loaded through the aft cargo door.

Figure 34 Error! No text of specified style in document.**:** Pallet Payload Configuration

8.9.3 Passenger/Paratrooper Transport

The aircraft can carry a maximum of 336 passengers in a 4-6-4 seat configuration. The passenger compartment is biased towards the aft of the aircraft to ensure a minimal change of static margin during flight. An optional paratrooper compartment can be included forward of the passenger compartment. Paratroopers are sat in rows 7 across for a total of 105 paratroopers in jump line formation. During a passenger-paratrooper configuration, paratroopers will egress through the aft cargo door by moving around the passenger compartment.

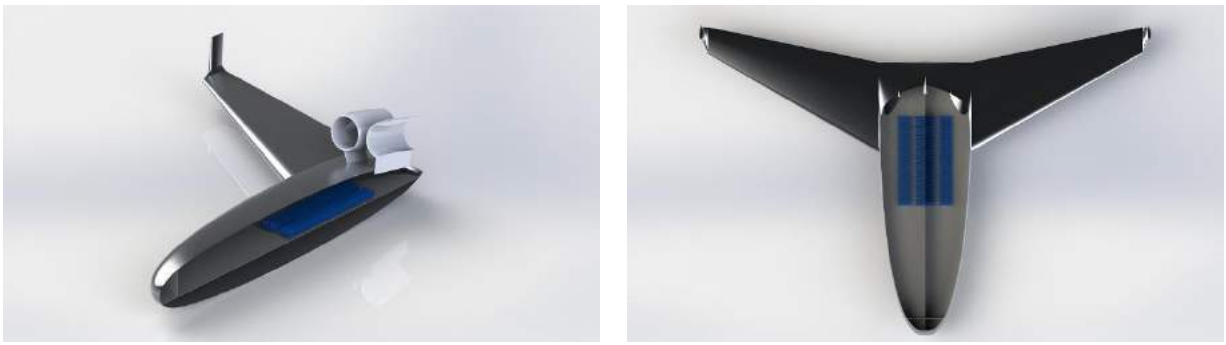

Figure 35 Error! No text of specified style in document.**:** Passenger Payload Configuration

8.10 Aircraft Access Points

The aircraft can be accessed through a large, actuated cargo door and ramp system that is located at the aft of the aircraft. This door will allow access for large cargo operations such as tanks and cargo pallets, as well as an egress point for parachuting operations. The main aft cargo door will include a telescoping ramp system to limit the loading angle to 12 degrees from horizontal.

For paratrooping operations where the aft cargo door is not available, 2 paratrooping floor chutes are available for paratrooper egress. Conventional side doors were not possible to include due to the aft placement of the wing, as any attempt to egress would encounter the leading edge of the wing. A top paratroop door was not considered due to the hazard of being ingested by the engines. Thus, a floor mounted door was chosen as the best solution. These chute doors guide the paratrooper through the lower portion of the fuselage in “slide” form, allowing for safe egress of the aircraft. These are to be only used when the aft cargo door cannot be used. The paratroop chutes cannot be used if the aft cargo door is opened during flight due to collision risks.

Two forward side doors allow access to the payload bay from the front of the aircraft and access to the cockpit. These doors are equipped with air stair units to allow entry into the aircraft without ground support units.

8.11 Cockpit Layout

Aircraft piloting will be conducted in a pressurized cockpit forward of the payload bay. The aircraft will be controlled by a traditional center column yoke which provides roll and pitch authority. The yoke will also include pitch, roll trim, autopilot disengage, and push-to-talk control. Rudder will be controlled through traditional foot pedals.

The cockpit layout uses a dark cockpit philosophy, meaning that during normal system operations, no lights are illuminated on the front panel and overhead panels. Each cockpit component is “hot swappable” such that a single system can be isolated and replaced in the event of a failure. Each pilot will have access to two LCD wide display units, each serving as the primary flight display (PFD) and navigation display (ND) unit, respectively. Modes can be toggled by each pilot for system redundancy. The center console display unit will primarily serve as the engine crew alert systems (ECAS) display and show flight critical alerts as well as systems health and status. This display can be toggled similar to the PFD and ND for redundancy in case of a display failure. Left and right avionics systems are independent of each other for additional redundancy. Additionally, steam gauge (analog) airspeed, altimeter, navigation, and attitude indicators are included in the center front panel for analog redundancy.

The mode control panel (MCP) controls all autopilot functions. Separate from the rest of the cockpit, the MCP follows a lights-on philosophy, meaning that active autopilot modes are illuminated. Lateral control modes include heading hold, GPS lateral navigation (LNAV), radio lateral navigation, and approach functions. Vertical control includes flight level change (constant airspeed or Mach number), vertical speed, or vertical navigation (VNAV). The aircraft will also include an autothrottle system to reduce pilot workload. Radio navigation and communication selection will also be included in the MCP for ease of access. The cockpit will also include a heads-up display (HUD) for low visibility operations and to reduce pilot workload. This system will be mounted above the pilot similar to the

787 and can be stored when not in use. The overhead display will contain control over all aircraft systems including electrical, hydraulic, fuel, air, engines, APU, and control of all standby systems and instrumentation.

The center console placed in between the captain and first officer (FO) seats will include one throttle quadrant with speed brake and flaps control, including fuel cutoff and fire suppression systems. All engines are FADEC, and the pilots do not have any manual authority over engine control. On either side includes two flight management system (FMS) displays which serve as the primary flight computer displays and interaction point for the aircraft. Aft of the center console will include all radio, transponder, and navigation control and redundancies, as well as 2 more standby FMS displays for redundancy.

The left and right sides of the captain and first officer seats, respectively, house the tiller, emergency oxygen masks, and window controls. Just aft of the cockpit is the circuit breaker panel, crew relief quarter, 2 jump seats and an observer's seat for relief crew. The relief quarter includes two beds, a bathroom, and a hot water dispenser. The cockpit is entered from the forward bulkhead. Figure 36 shows the general cockpit layout if seen from behind the captain and first officer chairs.

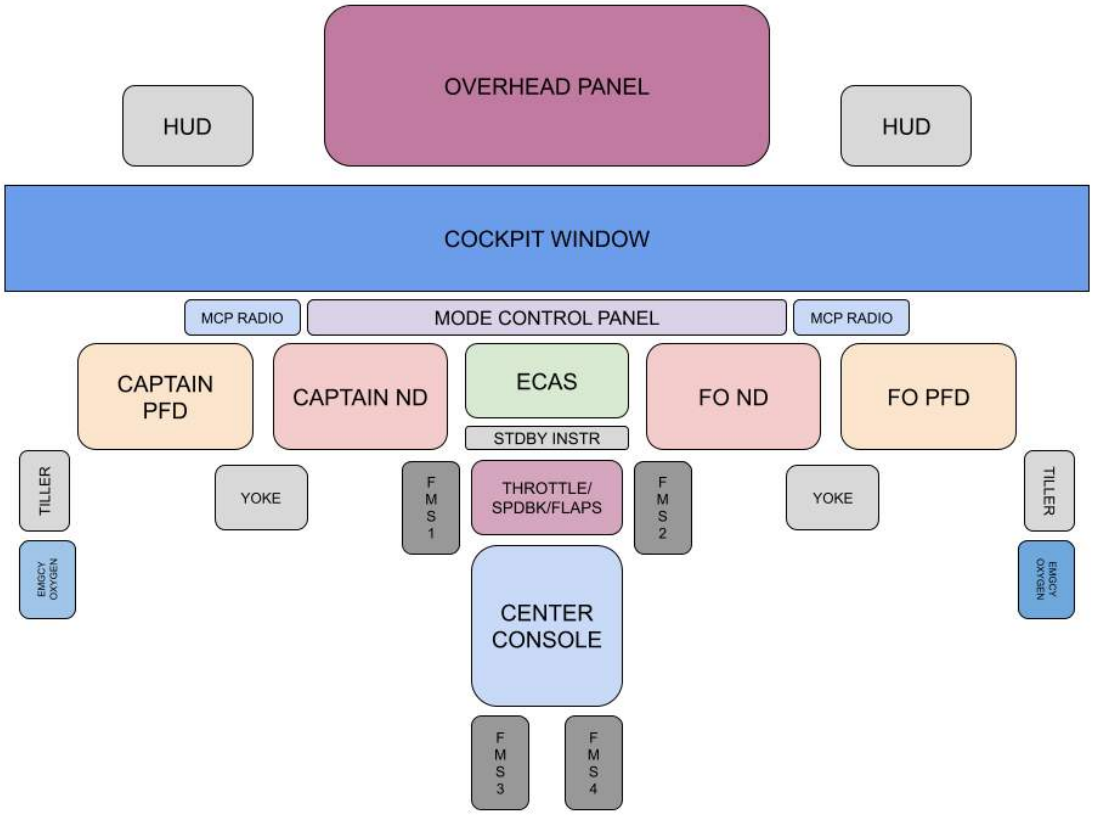

Figure 36 Error! No text of specified style in document.**:** General Cockpit Layout

8.12 Additional Instrumentation and Countermeasures

The aircraft includes commercial off-the-shelf avionics including weather radar, GPS, INS, and TACAN. A terrain following radar is also included for safety and low visibility operations. Installed radios are VHF/UHF transceivers, IFF transponder, and a SATCOM, all with redundant systems in case of avionics failure. The aircraft also includes a radar warning suite. Heat-seeking missiles, radar guided Surface to Air Missile (SAM) and Air to Air Missile (AAM) protection is provided through chaff and flare deployment stored in underwing compartments near the blended root.

9 Weight and CG Limits

With all aircraft components selected, and updated aircraft empty weight breakdown is presented below. The changes reflect the selection of specific engines and APU.

Table 19: Final Aircraft Weight after Component Selection

Component	Weight [kg]
Fuselage (Structural)	35700
Wing (Structural)	53500
Landing Gear Weight	18100
APU Weight (PW980)	450
Engines (3x GE9X)	28900
Instrumentation	5000
Hydraulics	2000
Climate Control Systems + Ducting	2570
Total Empty Weight	**14600**

Using a moment balance analysis, specific static margins and CG locations for each mission were calculated at the beginning and end of the mission. Geometric planforms of each component were drawn out in an excel sheet, and component-wise centers of gravity were assumed to be the centroid of each geometric planform. These were summed to find the longitudinal and spanwise CG locations. Component locations were iterated until a statically stable configuration was achieved. Figure 37 shows the excel aircraft layout during the tank mission for balancing. The red and black checkered circle indicated the CG at the beginning of the mission, and the yellow and black checkered circle indicated the CG at the end of mission. The assumed neutral point is marked by the green triangle aft of the CG marks.

The end of the mission was defined as the zero-fuel aircraft condition for each given mission. Payload locations were chosen to ensure a positive static margin and maintain a forward static margin of under 28%. Starting and ending static margins are tabulated in Table 20. In all but one case, the CG moves forward during flight due to the fuel burn in the swept wings. The CG moves aft in the paratrooper drop case due to the placement of the paratrooper compartment forward

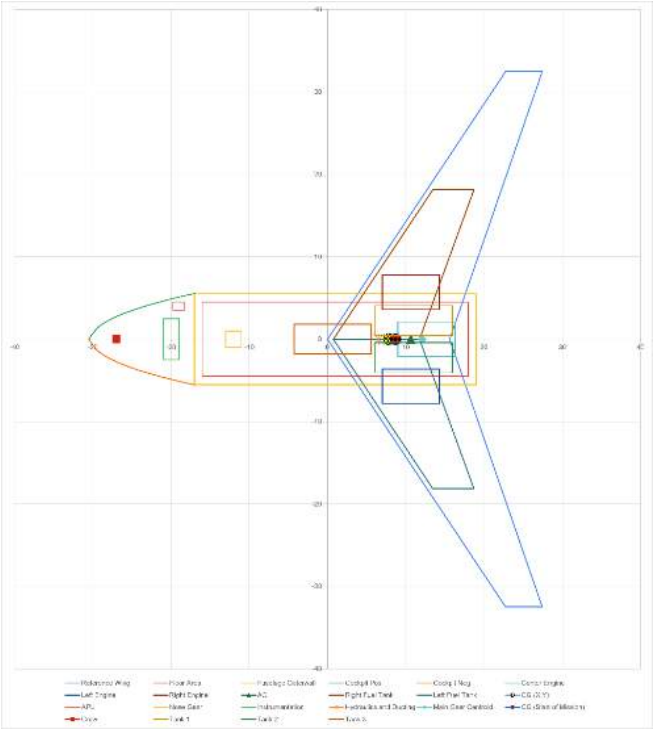

Figure 37 Excel Balance Layout of Caladrius during the Tank Transport Mission

of the passenger compartment. The specifics on control derivatives will be discussed in a following section. In all cases, passive static stability is met.

Table 20: Mission specific CG Locations for each mission

Mission	Static Margin: Start of Mission [% MAC]	CG Location: Start of Mission [m from nose]	Static Margin: End of Mission [% MAC]	CG Location: End of Mission [m from nose]
Ferry	3%	40.8	19.1%	39.0
Tank (3x M1A2)	17.7%	39.2	24.5%	38.4
Pallet (188000 kg Payload)	11.6%	39.9	17.7%	39.2
Passengers with Paratroopers	14.6%	39.5	12.3%	39.8
Passengers (Full)	14.6%	39.5	22.6%	38.6

10 Structural Design and Analysis

10.1 Structural Review

The carbon fiber fuselage and wings of the aircraft must sustain high-structural loading during nominal flight conditions through turns, takeoffs and landings. As such, these provide us with requirements that must be met for the fuselage and the wings to be structurally sound. The first requirement is the wings being able to withstand the stresses experienced, and the second requirement is for the structure to be lightweight. The latter, while being easier to deduce, is more challenging to get a picture of during initial design phases without extensive background work. The first is a more challenging consideration to include during primary structural design, but achievable and necessary. Stresses in composite materials are especially challenging to ascertain due to their non-isotropic properties, requiring diligent work to simulate the layup procedure within simulation which is difficult to model accurately without reliable and accurate manufacturing processes. To paint a realistic picture, conservative estimates were used wherever possible alongside a margin of safety factor to account for manufacturing uncertainty.

$$Factor\ of\ Safety\ (FoS) = \frac{Stress * 1.5}{Strength} \tag{23}$$

A safety factor of 1.50 was used as is standard in the Aerospace industry.

$$Margin\ of\ Safety\ (MoS) = \ Factor\ of\ Safety - 1.5 \tag{24}$$

10.2 Structural Materials

Toray T2510 was selected for the fuselage with the material properties presented in Table 21.

Table 21: Material Properties for Toray T2510 [22]

Material	Density ($kg\ m^{-3}$)	Orthotropic Elasticity (Pa)	Poisson's Ratio	Shear Modulus (Pa)
Toray T2510	1502	X: $5.62 * 10^{10}$	X: 0.0533	X: $3.89 * 10^{9}$
		Y: $5.62 * 10^{10}$	Y: 0.3	Y: $3.19 * 10^{9}$
		Z: $6.33 * 10^{9}$	Z: 0.3	Z: $3.19 * 10^{9}$

10.3 ANSYS ACP Setup

The ANSYS [23] Composites Prep/Post system was utilized as the preprocessor to achieve a simulation of a laminate by utilizing the orthotropic properties of each ply. The OpenVSP [18] file was used to populate the geometry section of ANSYS ACP with a model. Note: model has been sliced in half along a symmetrical line to reduce computation time. The model was then meshed utilizing a quad dominant method producing the result shown below.

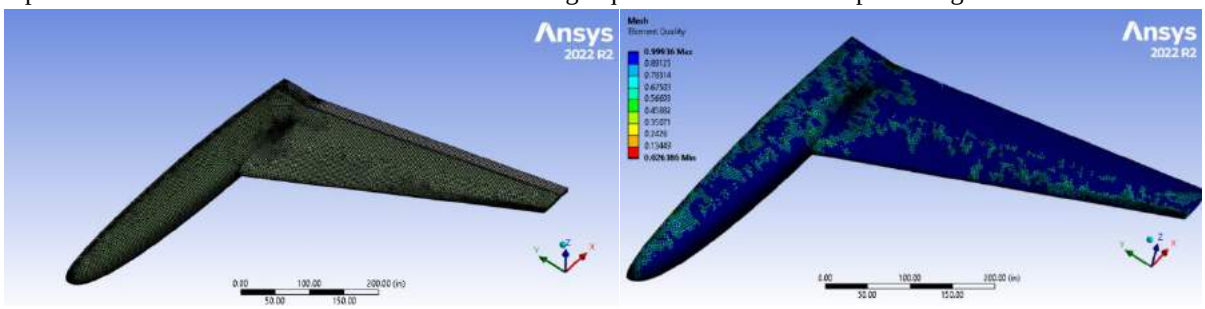

Figure 38. Multipart figure showing a quad dominant mesh alongside quality metrics

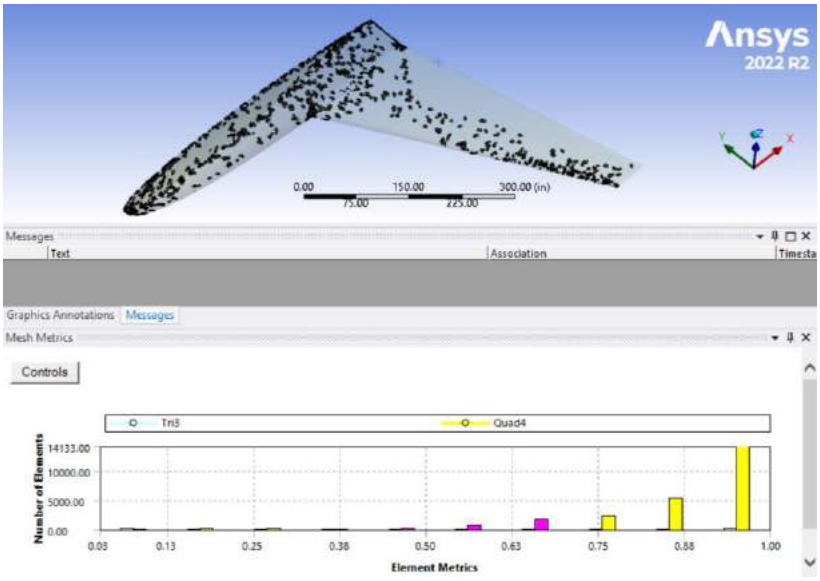

Figure 39. Detailed View of Mesh Metrics

A closer view of the mesh metrics highlights that the vast majority of elements are within a satisfactory quality, which is a very important metric to ensure anomalous results do not propagate within the simulation and skew overall findings.

Table 22. Element and Node totals Element Size, Number of Nodes

Average Element Size (In)	Number of Nodes	Number of Elements
3.34 in	25,072	24,757

Next, began the actual setup of the layup, within ACP and summarized parameters are shown below:

Table 23: Wing and Fuselage Ply Layup Schedule for Toray T2510 Plain Weave

Ply #	Angle	Nominal Thickness
1	45°	0.02 In per layer
2	90°	
3	45°	
4	90°	
5	45°	
6	90°	
7	45°	
8	90°	
9	45°	
10	90°	

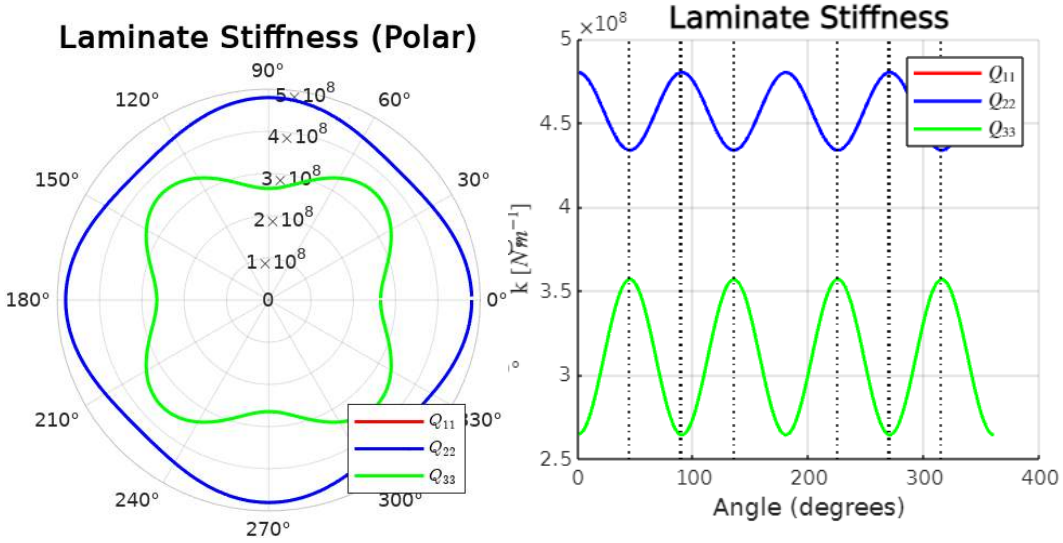

Figure 40: Laminate Stiffness Computed for the Ply Layup Schedule

To further validate the model, an empirical hand-calculation was carried out assuming a thin-walled cylindrical fuselage utilizing classical laminate theory. Promising deformation results were shown with very low strains of $2.01 * 10^{-4}$ and $7.78 * 10^{-4}$ inches and axial and hoop directions respectively.

10.4 Loading Conditions:

Maximum load factor given is by $n_{struct} = 3$, therefore the maximum aerodynamic loading on each wing can be estimated by

$$\frac{3 * MTOW}{2} = 1{,}345{,}922\ lbs\ of\ loading\ on\ each\ wing$$

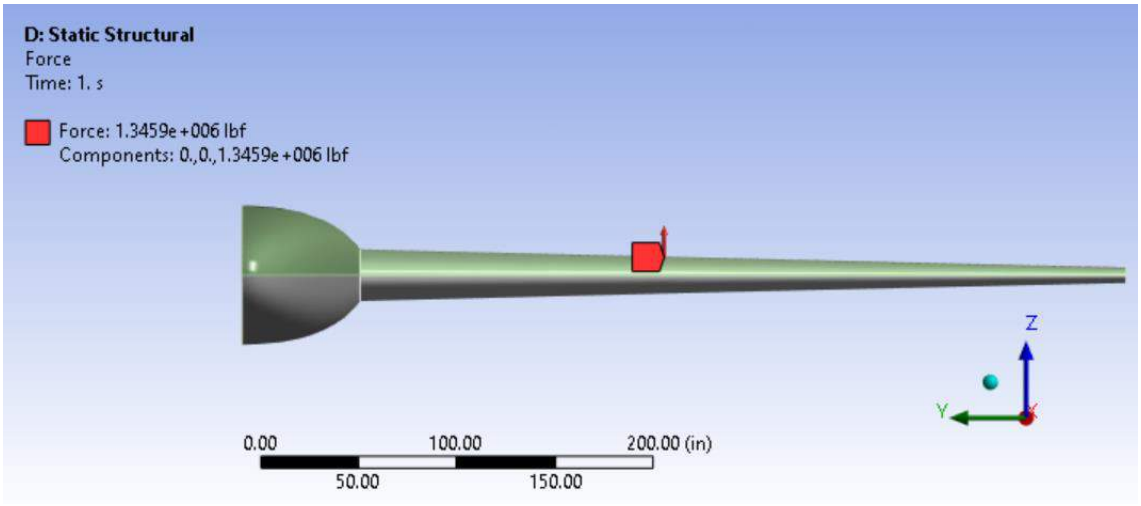

Figure 41: Load Setup for Max Turn Loading

This loading alongside the imported composite data onto the shell of the body gives us the full composite model. Finally the model was fixed on the edge length of the fuselage where the symmetrical cut was made.

10.5 Tsai-Wu Failure Method:

Before introducing results, it is important to ascertain the method as to which results are produced. Whilst most standard analysis involves getting the stress concentration and dividing that by the ultimate or the yield stress, within composite analysis this is not as simple. Composites have wildly different properties depending on the directions they are loaded and for the aircraft the way the loading propagates is not necessarily simple or in one direction therefore there have been empirical models which have been developed to investigate how these loadings will cause failures in composites. A common method used for composite shell bodies is the Tsai-Wu Failure Criterion.

$$F_1 = \left(\frac{1}{X_1^T} - \frac{1}{X_1^C}\right), F_2 = \left(\frac{1}{X_2^T} - \frac{1}{X_2^C}\right), F_{12} = -\frac{1}{2}\sqrt{\frac{1}{X_1^T * X_1^C} * \frac{1}{X_2^T * X_2^C}}\ ,$$

$$F_{11} = \frac{1}{X_1^T X_1^C}\ , F_{22} = \frac{1}{X_2^T X_2^C}, F_6 = \left(\frac{1}{X_{12}^T} - \frac{1}{X_{12}^C}\right), F_{66} = \frac{1}{{X_{12}}^T * {X_{12}}^C}$$

Figure 42. Tsai Wu Failure Criterion Governing Equations [37]

Fortunately, ANSYS ACP includes a way to get the simulation to use these Tsai Wu failure criterions within the simulation after defining the material's orthotropic stress limit and then giving a simple factor of safety (which is the

lower value of both the compressive and tensile loadings). For the results section below, all factors of safety are assumed to be derived from the Tsai Wu Failure Criterion.

10.6 Results

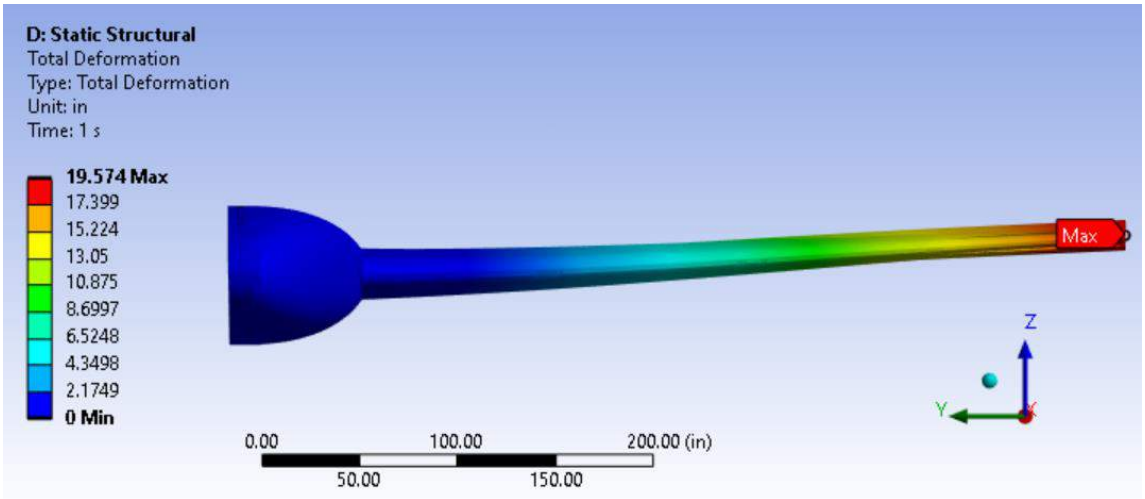

Figure 43. Deflection of Composite Wing under max lift loading

A deformation of 19.6 in was seen during the maximum load factor, this indicates that the analysis is reasonable as modern passenger airliners regularly deform a similar amount.

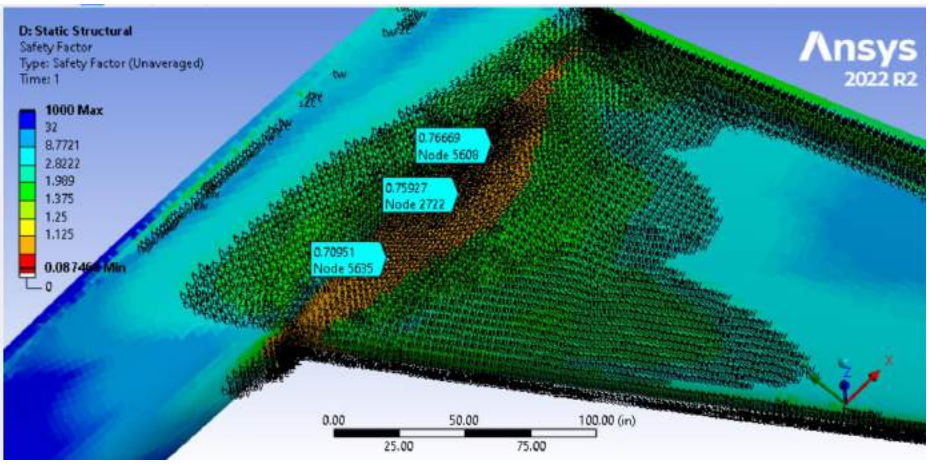

Figure 44. Tsai-Wu Factors of Safety on Various Positions of the Wing Before Iteration

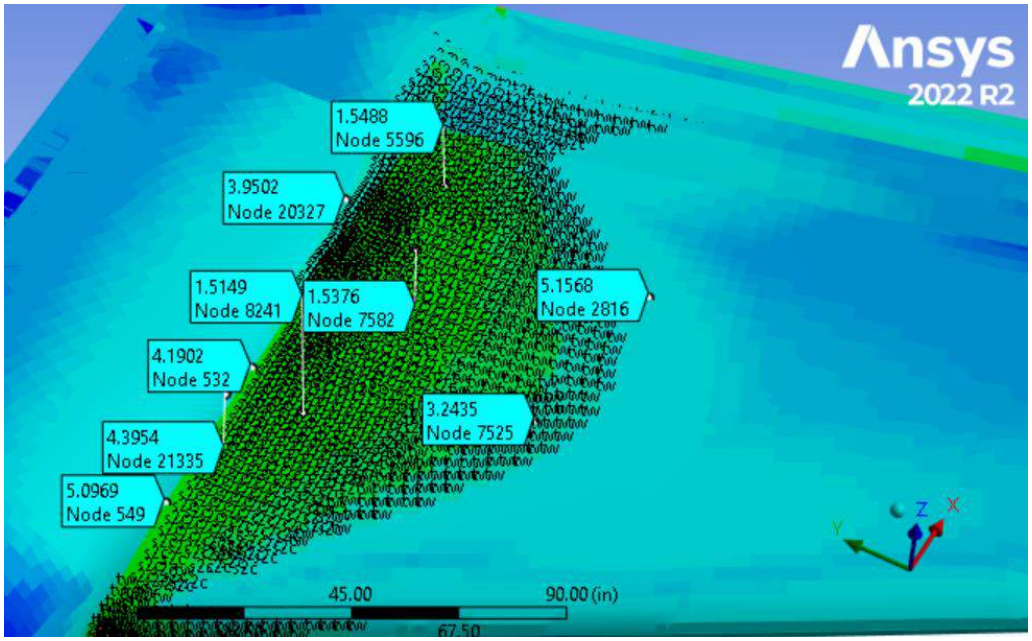

Figure 45. Tsai-Wu Factors of Safety on Various Positions of the Wing After Iteration

Our results indicate a positive of safety for the wing body suggesting that this design is suitable structurally to carry expected loads. Our lowest factor of safety and thus by correlation the highest stress concentrations appear to be found in the region between the wing and the fuselage likely due to bending loads. These positive results were achieved after iterating through various different thickness of plies (0.01-0.02, each individual ply).

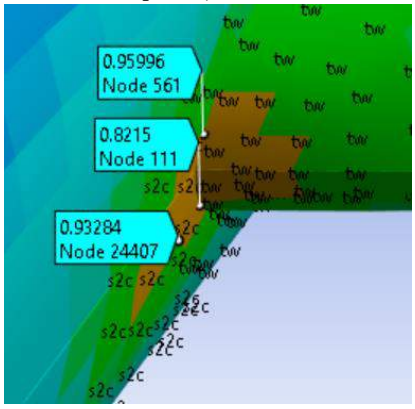

Figure 46. Identification of Problematic Factors of Safety

Unfortunately, negative factors of safety were found within the fillets of between the wing and fuselage and this is also where the aircraft would expect the highest stress concentrations. These stresses are likely due to contact stresses created by the fixed constraint between the wing and the fuselage. To mitigate these stresses the Caladrius Group intends to reinforce the area, giving a higher cross section thus reducing stresses. The model currently analyzed did not have these extra reinforcements but with them a positive margin of safety is to be expected thus clearing the aircraft to fly structurally.

10.7 Structural Analysis Summary

Table 24. Summary of Structural Results:

Component	Area	Equivalent Stress (psi)	Factor of Safety (FoS, Tsai-Wu)	Margin of Safety (MoS)
Wings	Wing Body	3,940	10.1	8.60
	Leading Edge	10,500	4.44	2.94
	Trailing Edge	12,500	3.62	2.12
	Root	32,400	1.52	0.02
	Fillets (Will be addressed with reinforcements)	$1.69 * 10^5$ (stress singularity)	0.83	-0.67
Fuselage	Nose	1.01	>1000	>1000
	Fuselage Body	1,470	34.2	32.7
	Aft Fuselage	2,310	20.7	19.2

Overall the structure has been optimized by iterating and ensuring that the thickness of the fuselage and wing bodies stay low thus reducing the weight component of the vehicle. Future structural optimizations would be to confirm the fillet reinforcements and simulate other loading conditions.

10.8 Manufacturing Plan

This aircraft is comprised of plain weave carbon fiber with a Toray 2510 prepreg system. This bidirectional material is suitable for autoclave or oven cures, which allows flexibility in the manufacturing process [22]. For example, when manufacturing smaller components like the winglets, they can be cured in an oven while larger sections of the vehicle for the main body can be done in an autoclave. Autoclaves decrease porosity (voids), leaving a smoother finish to impede drag penalties [24]. Also, because of autoclaves' high pressure and heat, the individual laminates bond better, resulting in a lighter and stronger part [25]. On top of that, this epoxy resin system was deemed the most advantageous in comparison to, for example, a phenolic epoxy system, which is more expensive and has a more complex curing cycle due to the generation of water; the only advantage is its high heat resistance [26], although this isn't prioritized as the aircraft doesn't require resistance to fire.

In manufacturing, due to the shape of blended wings, the vehicle will be laid up (with a +- 45, 90-degree ply orientation) in sections of the aircraft's main body and individually lay up the winglets sections where the geometry drastically changes. These different sections will then be connected with the Kevlar thread. Kevlar thread can withstand multidirectional stress in contrast to traditional aluminum manufacturing methods [27]. Additionally, as this vehicle is competently made from composites, the plane will be lightweight and have fewer overall parts, signifying a decrease in points of failure and fewer components needed to be manufactured. Jet Zero, which is currently developing a blended wing that moves away from metal and composites to principally carbon fiber stitched together with Kevlar, reflects this same manufacturing layout [28]. The only large difference is that they are

utilizing non-prepreg material and choosing to add epoxy resin at a later step. This technique of kevlar stitching is effective with either type of fiber [27]; thus, it isn't a design concern.

11 Cost Analysis

Cost analysis plays a crucial role in aircraft design. Considering the target market and expediated delivery date for the project, an economic evaluation is critical. The cost analysis is split into Research Development Test and Evaluation (RDTE) costs, production costs, tooling cost, and development support costs cited from Raymer [7].

11.1 Methods and Assumptions Applied

Estimating the cost of developmental aircraft is a very difficult task but can be made simpler depending on the method used and assumptions made. In the cost analysis model for Caladrius, the DAPCA IV model was used from Raymer [7]. This model uses estimates on the cost per hour on RDTE and production on engineering, tooling , manufacturing, and quality control.

The assumptions made for the cost analysis were factoring an empty weight of 141,000 kg, a max velocity of 472 kts, initial production quantity of 2 aircraft, 2 produced flight test aircraft, three engines per aircraft, max thrust of 21,936 lbs, max Mach of 0.85, temperature of turbine inlet 2,164 R, and the avionics cost of $138,300,000.

11.2 Total Costs

Table 25: Total fixed costs for 2 units

Variable	Cost per unit [$]
Total engineering cost	3,760,053,700
Total tooling cost	1,506,021,775
Total manufacturing cost	933,919,438
Total development cost	788,685,762
Total materials cost	201,407,150
Total cost	7,374,064,407

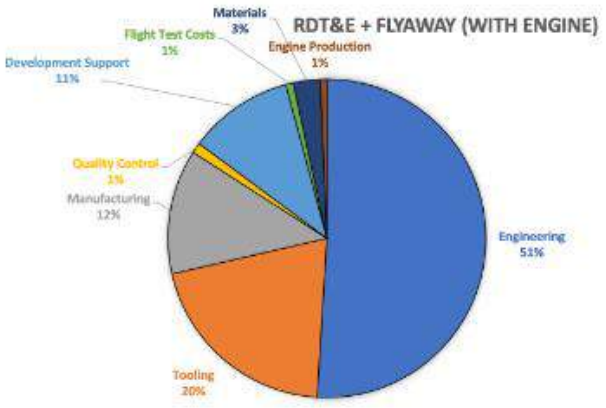

Figure 47 Identification of Problematic Factors of Safety

Table 24 reveals that the total estimated cost for one Caladrius aircraft in USC 2023 is projected to be $1,843,516,000. A close examination of the data also highlights that the majority of the design costs are attributed to engineering expenses. This substantial allocation suggests the high level of technical expertise and advanced innovation required to bring Caladrius to fruition. The investment in engineering is critical for achieving the desired performance and capabilities of the Blended Wing Body (BWB) design, ensuring the aircraft's operational effectiveness and efficiency. It should also be noted that these values are assumed for general aircraft and the BWB design is a conceptual design with no truly allocated manufacturing costs.

12 Lifecycle Emissions

Today, 4 percent of the global carbon dioxide emissions are from aircraft whose propellants consist of carbon dioxide (CO2) and Nitric Oxide (NOX), showing the importance of reducing new aircraft emissions in combatting climate change [29]. Therefore, this aircraft is powered by GE9X engines that operates utilizing a 100% sustainable aviation fuel (SAF) blend, which is composed of nonpetroleum feedstocks. The main principle behind the SAF fuel is that it uses carbon currently in the carbon cycle from sources such as food, woody biomass, fats/grease, and household waste instead of taking stored carbon and putting it in the atmosphere. On average, there is an 80% decrease in carbon dioxide emissions [30] with SAF compared to traditional fossil fuels jet fuel [31]. On top of that, the GE9X engines produce only 45% of the regulatory nitrogen oxide requirements due to decreased combustion temperatures, which also have a smaller radiative forcing impact, which tends to influence or worsen global warming [32].

Figure 48. SAF Fuel Manufacturing and Processing [38]

In terms of emissions produced due to the material required for manufacturing, this blended wing is composed of carbon fiber, which have decreased CO_2 emissions compared to other materials such as aluminum. It has been found that when an aircraft fuselage is only 50% carbon fiber reinforced polymer (CFRP), a 27,000 ton—or 7 percent—decrease in CO_2 emissions occurs [33]. However, that is with the consideration of only the full life cycle emissions. When only analyzing the manufacturing process, carbon fiber can have high energy requirements to impregnation of resin and curing processes, resulting in increased environmental impact compared to materials like

aluminum alloys or steel. Nevertheless, because of carbon fiber's lightweight nature, far less fuel is required for missions, which have been shown to more than offset the manufacturing effects on the environment [34].

On top of that, there are numerous methods to recycle carbon fiber to decrease the emissions that have been developed. For example, mechanical recycling, where the CFRP has an average 24% recycling rate, consists of cutting/shredding the composite into smaller pieces to be later reused. On top of that, other methods like pyrolysis can result in a 65% average fiber recovery rate, resulting in dry fiber that can be implemented in other projects instead of being sent to landfills [34].

Additionally, looking towards manufacturing the Toray Carbon Fiber specifically chosen for this aircraft, this company emphasizes reducing emissions. Its largest steps towards its goal include expanding its renewable energy factories and carbonless electricity at plants. For example, as of 2022, there were 5 Toray plants along with 20 affiliated overseas that had instead renewable energy, with other offices also having carbon-free power sources, such as the Tokyo Head Office, which resulted in a 1500 tones Co_2/year decrease [36]. As a result of these efforts and more in 2022, Toray company reduced by 35% its greenhouse emissions per unit revenues in comparison to 2013 [36].

Hence, overall, carbon fiber has been determined to be the most optimal choice when decreasing greenhouse emissions into the atmosphere, from manufacturing the carbon fiber to implementing the carbon for the layup and the recycling procedures.

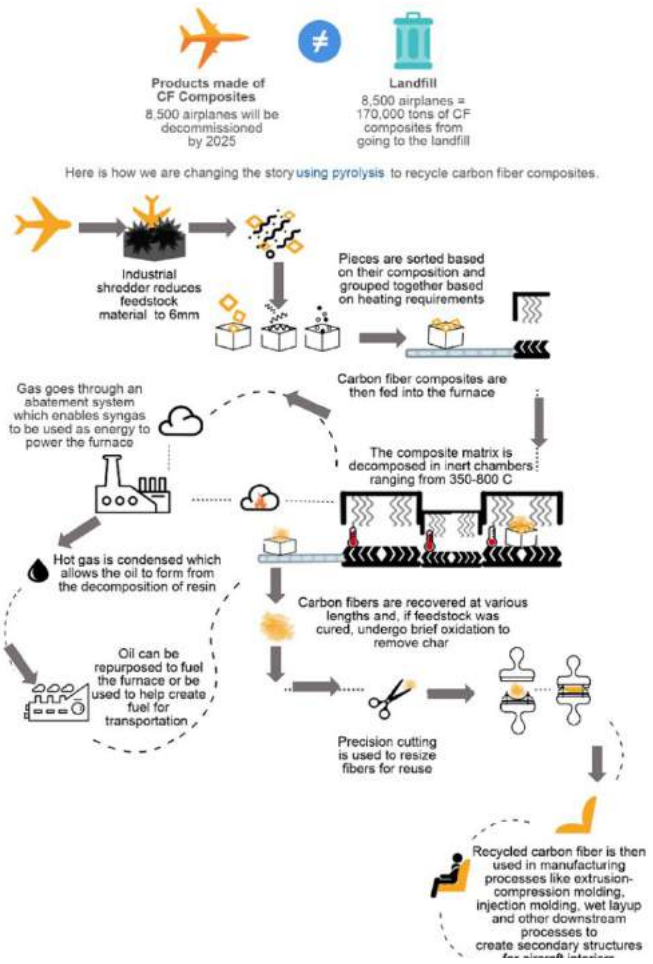

Figure 49: Carbon Fiber Manufacturing [35]

13 Conclusion

The Caladrius design, as presented in this report, has the potential to improve the range, endurance, and payload-weight capabilities of the USAF HLA fleet with improved aerodynamic and propulsive capabilities, combined with state-of-the-art manufacturing and aerospace technology. Primary future steps in the development of Caladrius would include more detailed design, including structural analysis of the wing and fuselage assembly, as well as integration of all key subsystems.

Appendix A –
Caladrius 3-View

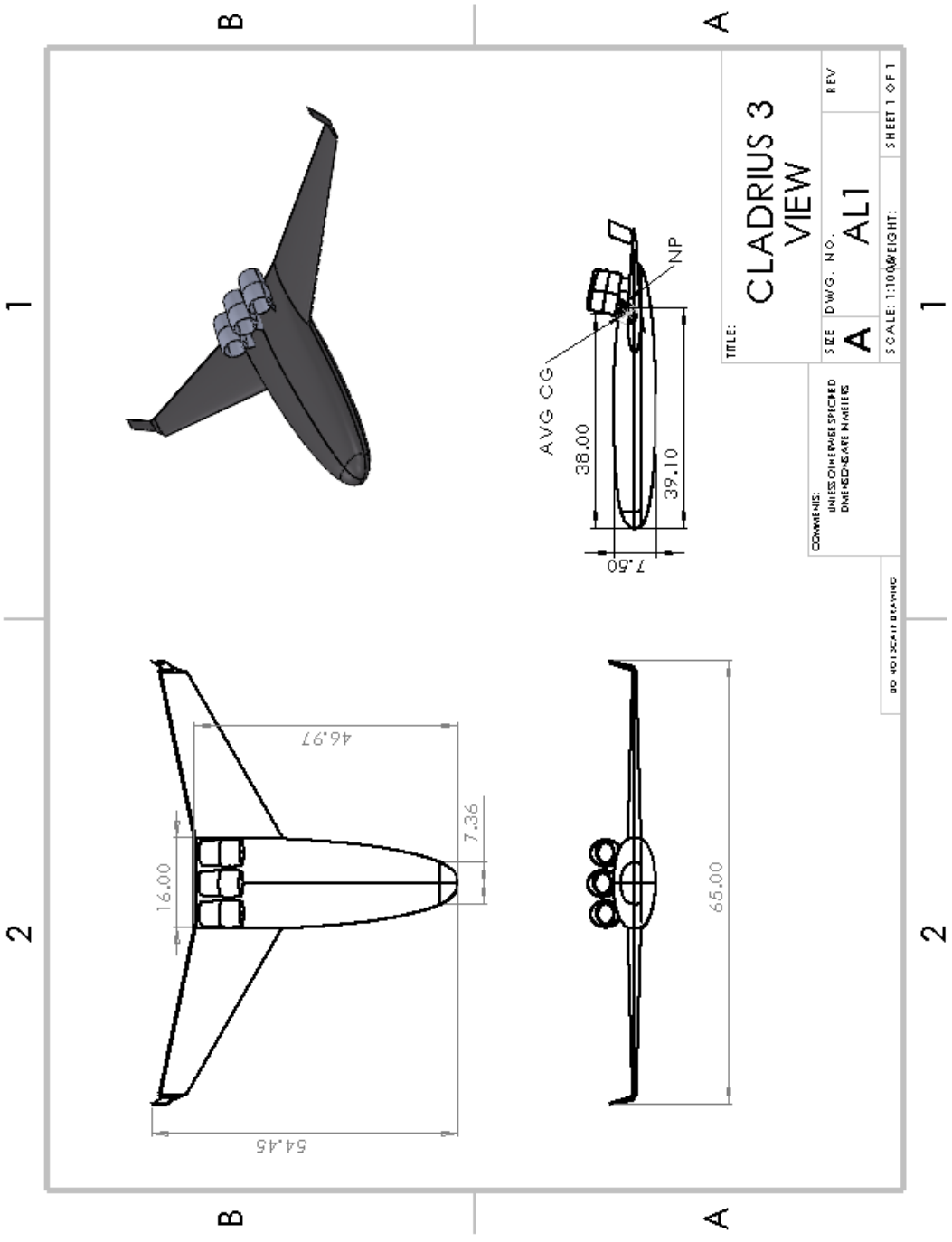

Figure 50. Identification of Problematic Factors of Safety

Appendix B –
Numerical and Analytical Model Comparison

The time-based models described in Sections 3 were compared to corresponding analytical models. First, the takeoff model was compared with Eq. 9 for the designed aircraft at several altitudes and various weight configurations. The results are shown in Figure 51 with the time-based model plotted as solid lines.

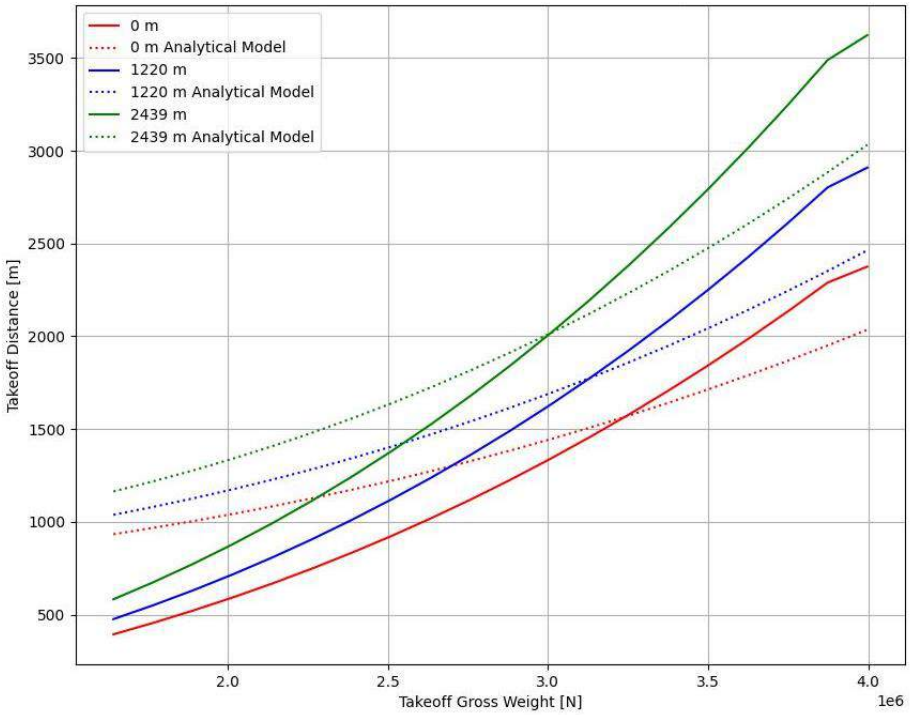

Figure 51: Comparison of Time Based and Analytic Balanced Field Length Takeoff Models

The time-based model has a greater range of takeoff distances, exceeding those predictions of the analytical model at higher weights, and predicting much better takeoff performance at low weights than the analytical model. This is likely because the analytical model is statistical model and therefore developed for typical jet aircraft; therefore, it is reasonable to assume that this model will not predict performance of HLA aircraft entirely accurately. Because of these variations between the models, the time-based model was used exclusively in this report because it provided a more conservative estimate of takeoff performance.

The time-based cruise model was also compared with the analytic model given by Eq. 10. Because the lift coefficient varies in flight with changing weight, as demonstrated by Figure 12, the compressible parasitic drag correction, ΔC_D, also changes. Therefore, when using the analytic model, the average lift coefficient during cruise was used for drag calculations. Table X shows the time-based and analytic cruise ranges for various cruise altitudes and weights. All scenarios assumed a cruise at Mach 0.8.

Table 26: Comparison of **Time-Based** and *Analytical* Cruise Models

Altitude	Weight		
	407,000 kg	**314,000 kg**	**213,000 kg**
9,500 m (31,000 ft)	**20,020 km** *20,020 km*	**20,030 km** *20,030 km*	**12,830 km** *12,830 km*
10,700 m (35,000 ft)	**21,270 km** *21,470 km*	**21,270 km** *21,470 km*	**13,840 km** *13,960 km*
11,900 m (39,000 ft)	**21,940 km** *22,300 km*	**21,940 km** *22,310 km*	**14,610 km** *14,790 km*

Note: time-based model values are given in **bold** and analytic model values are given in *italics*

At lower altitudes, there is very good agreement between the analytic and time-based model (less than 1km difference). This is because ΔC_D varies very little during cruise because the coefficient of lift is low enough to make this drag term negligible (again, a cruise at Mach 0.8 was assumed, meaning that a lower coefficient of lift was required at lower altitudes because of the higher air density). This means that parasitic component of drag, which the analytic model assumes to be constant, varies negligibly during cruise, and therefore there is no significant difference between the time-based and analytic models. However, at higher altitudes, a higher lift coefficient is required for a same given true airspeed, and therefore compressible drag becomes non-negligible. The analytic model tends to yield a longer range here because it uses the average lift coefficient, not capturing the non-linear dependence of ΔC_D on the lift coefficient.

To demonstrate the inability of the analytic model to capture dynamic parasitic drag behavior, Table 27 shows the results of the same study but with the analytic model using the parasitic drag computed at the start of cruise where the compressible drag term will be at its highest during flight.

Table 27: Comparison of **Time-Based** and *Analytical* Cruise Models with Adjusted Drag Modelling

Altitude	Weight		
	407,000 kg	**314,000 kg**	**213,000 kg**
9,500 m (31,000 ft)	**20,020 km** 19,730 *km*	**20,030 km** *19,740 km*	**12,830 km** *12,737 km*
10,700 m (35,000 ft)	**21,270 km** *20,880 km*	**21,270 km** *21,470 km*	**13,840 km** *13,820 km*
11,900 m (39,000 ft)	**21,940 km** *20,071 km*	**21,940 km** *20,072 km*	**14,610 km** *14,490 km*

As expected, the analytical model predicts lower ranges at all configurations because it overpredicts the parasitic drag coefficient. In fact, at higher altitudes, the analytic model predicts a decrease in range compared to lower altitudes because of the nonlinear increase in the compressible drag term. This highlights the key limitation of the analytic range in its inability to capture the dynamic compressible drag effects; therefore, the time-based cruise model was used exclusively in this report.

Appendix C –
Numerical Methods

The codebase used for trade studies contained in this report can be accessed here. The code is considered proprietary and should not be redistributed in any manner or form without the expressed written consent of the authors of this paper. The authors thank you for your cooperation.

The authors of this paper would also like to take this opportunity to state that they have no conflicts of interests that impacted the content and publication of this report.

Bibliography

[1] Okonkwo, Paul (1995). “Review of evolving trends in blended wing body aircraft design.” Progress in Aerospace Sciences, 31. https://www.sciencedirect.com/science/article/abs/pii/S0376042115300336
[2] Chen, Z., Zhang M., Chen Y., Sang W. Tan Z., Li D., Zhang B. (2019). Assessment on Critical Technologies for Conceptual Design of Blended-Wing-Body Civil Aircraft. *Chinese Journal of Aeronautics, 32(8).* https://www.researchgate.net/publication/334518797_Assessment_on_critical_technologies_for_conceptual_design_of_blended-wing-body_civil_aircraft
[3] Aircraft Grade Aluminum (2023). *Materials Services.* https://www.thyssenkrupp-materials.co.uk/aircraft-grade-aluminum#:~:text=Aluminum%20plays%20a%20vital%20role,its%20resistance%20to%20UV%20damage
[4] Pros and Cons of Composite Materials: Pacific Aerospace Corp (2021). *Pacifc Aerospace Corp (PAC).* https://www.pacificaerospacecorp.com/what-are-the-pros-and-cons-of-composite-materials/
[5] Aluminum vs Steel for Manufacturing Airplanes: Which Is Best? (2019). *MONROE AEROSPACE.* https://monroeaerospace.com/blog/aluminum-vs-steel-for-manufacturing-airplanes-which-is-best/#:~:text=Weight,more%20desirable%20material%20for%20airplanes
[6] Gudmundsson, S., General Aviation Aircraft Design: Applied Methods and procedures, Oxford: Butterworth-Heinemann, 2022
[7] D. Raymer, in *Aircraft Design: A Conceptual Approach*, Reston, Virginia, AIAA, 1999.
[8] Aeronautical Information Manual. *FARAIM.* https://www.faraim.org/faa/aim/index.html
[9] scipy.integrate.solve_ivp. *SciPy API.* https://docs.scipy.org/doc/scipy/reference/generated/scipy.integrate.solve_ivp.html
[10] Python. [Online]. Available: https://www.python.org//
[11] *14 CFR Chapter I - FEDERAL AVIATION ADMINISTRATION, DEPARTMENT OF TRANSPORTATION*. (2019). LII / Legal Information Institute. https://www.law.cornell.edu/cfr/text/14/chapter-I
[12] J.D. Mattingly, W.H. Heiser, D.T. Pratt, Aircraft Engine Design, 2nded., AIAA Education Series, 2002.
[13] Holder, T. (2022). *TYPE-CERTIFICATE DATA SHEET for Trent 1000 series engines*. *EASA.* https://www.easa.europa.eu/en/downloads/7733/en
[14] Hoak, D., and Ellison, D., et al., "USAF DATCOM," Air Force Flight Dynamics Lab., Wright-Patterson AFB, OH.
[15] M. Drela and H. Youngren, "AVL," 2017. [Online]. Available: https://web.mit.edu/drela/Public/web/avl/.
[16] "XFLR5," 2019. [Online]. Available: http://www.xflr5.tech/xflr5.html.
[17] *Dynamic Regulatory System* (2023). *U.S. Department of Transportation.* https://drs.faa.gov/browse/excelExternalWindow/DRSDOCID1144837364202302031810002.0001?modalOpened=true
[18] OpenVSP 2024. [Online]. Available: https://openvsp.org/
[19] XFOOIL 2024. [Online]. Available: https://web.mit.edu/drela/Public/web/xfoil/
[20] Aircraft Charecteristics Airport And Maintenance Planning (2020). Airbus. https://www.airbus.com/sites/g/files/jlcbta136/files/2021-11/Airbus-Aircraft-AC-A380.pdf
[21] Goodyear Aviation Data Book (2022). Goodyear Aviation. https://www.airbus.com/sites/g/files/jlcbta136/files/2021-11/Airbus-Aircraft-AC-A380.pdf
[22] *2510 Prepreg System Data Sheet PRODUCT NOTES*. (n.d.). Retrieved May 8, 2024, from https://www.toraycma.com/wp-content/uploads/2510-Prepreg-System.pdf
[23] ANSYS 2024. [Online]. Available: https://www.ansys.com/
[24] *Autoclave Cure*. (n.d.). Toray Composite Materials America, Inc. https://www.toraycma.com/applications/autoclave-cure/#:~:text=Autoclave%20curing%20of%20composites%20applies
[25] Autoclave Molding (2011). *Polymer Matrix Composites and Technology.* https://www.sciencedirect.com/topics/materials-science/autoclave-molding#:~:text=This%20process%20has%20some%20advantages,well%20as%20high%2Dquality%20products
[26] Phenolic Resin (2013). *Themoplastics and Thermoplastic Composites.* https://www.sciencedirect.com/topics/chemical-engineering/phenolic-resin#:~:text=Phenolics%20are%20of%20particular%20interest,involves%20the%20generation%20of%20water
[27] Ogin, S., Potnuri, P. (2016). Composite Stiching. *Handbook of Technical Textiles.* https://www.sciencedirect.com/topics/materials-science/composite-stitching

[28] Karlin. S (2023). How JetZero aims to be the 'SpaceX of aviation'. *FASTCOMPANY.* https://www.fastcompany.com/90902351/how-jetzero-aims-to-be-the-spacex-of-aviYation
[29] Life Cyclye of Energy in Aviation. *NASA*. https://www.nasa.gov/wp-content/uploads/2023/08/lifecycle_of_energy-9-12.pdf)
[30] Sustainable aviation field (2024). *AIRBUS.* https://www.airbus.com/en/sustainability/respecting-the-planet/decarbonisation/sustainable-aviation-fuels#:~:text=SAF%20is%20one%20of%20the,lies%20in%20its%20life%20 cycle.).
[31] Belger, R (2020). Sustainable Aviation Fuels.
Sustainable Aviation Fuels | Roland Bergerrolandberger.comhttps://www.rolandberger.com › publication_pdf › rolan...)
[32] Born of power and efficiency. *GE Aerospace*. (https://www.ge.com/news/sites/default/files/2023-11/ge-ge9x-rr_final2.pdf
[33] Life Cycle Assessment. *TORAY*. https://www.cf-composites.toray/aboutus/sustainability/lci.html#:~:text=Carbon%20fiber%20is%20an%20environmentally,1%20ton%20of%20carbon%20fiber.
[34] Yagmur Atescan-Yuksek, Mills, A., Ayre, D., Koziol, K., & Konstantinos Salonitis. (2024). Comparative life cycle assessment of aluminium and CFRP composites: the case of aerospace manufacturing. *The International Journal of Advanced Manufacturing Technology*. https://doi.org/10.1007/s00170-024-13241-3
[35] Kooduvalli K, Unser J, Ozcan S, Vaidya UK. Embodied Energy in Pyrolysis and Solvolysis Approaches to Recycling for Carbon Fiber-Epoxy Reinforced Composite Waste Streams. *Recycling*. 2022; 7(1):6. https://doi.org/10.3390/recycling7010006
[36] Materials Change Our Lives (2023). *Toray Group.* https://www.toray.com/global/sustainability/tcfd/pdf/TCFD_report_v2.pdf
[37] *Tsai-wu failure criterion*. SOLIDWORKS Help. (n.d.). https://help.solidworks.com/2021/English/SolidWorks/cworks/r_tsaiwu_failure_criterion.htm
[38] What is sustainable aviation fuel? (2022). *Air bp*. https://www.bp.com/en/global/air-bp/news-and-views/views/what-is-sustainable-aviation-fuel-saf-and-why-is-it-important.html